# Species-specific differences in nonlysosomal glucosylceramidase GBA2 function underlie locomotor dysfunction arising from loss-of-function mutations

Received for publication, October 16, 2018, and in revised form, January 16, 2019 Published, Papers in Press, January 20, 2019, DOI 10.1074/jbc.RA118.006311

**Marina A. Woeste[‡1], Sina Stern[§1], Diana N. Raju[‡], Elena Grahn[¶], Dominik Dittmann[‡], Katharina Gutbrod[‖], Peter Dörmann[‖], Jan N. Hansen[‡], Sophie Schonauer[¶], Carina E. Marx[¶2], Hussein Hamzeh[¶], Heinz G. Körschen[¶], Johannes M. F. G. Aerts[**], Wolfgang Bönigk[¶], Heike Endepols[‡‡], Roger Sandhoff[§§¶¶], Matthias Geyer[‖‖], Thomas K. Berger[¶3], Frank Bradke[§3], and Dagmar Wachten[‡¶3,4]**

*From the [‡]Institute of Innate Immunity, University Hospital, University of Bonn, 53127 Bonn, Germany, the [§]German Center for Neurodegenerative Diseases (DZNE), 53127 Bonn, Germany, the [¶]Center of Advanced European Studies and Research (Caesar), 53175 Bonn, Germany, the [‖]Institute of Molecular Physiology and Biotechnology of Plants, University of Bonn, 53115 Bonn, Germany, the [**]Leiden Institute of Chemistry, Leiden University, 2333 CD Leiden, The Netherlands, the [‡‡]Institute of Radiochemistry and Experimental Molecular Imaging (IREMB) and Department of Nuclear Medicine, University Hospital of Cologne, 50937 Cologne, Germany, the [§§]Department of Cellular and Molecular Pathology, German Cancer Research Center, Heidelberg, Germany, the [¶¶]Lipid Pathobiochemistry Group, German Cancer Research Center, 69120 Heidelberg, Germany, and the [‖‖]Institute of Structural Biology, University Hospital, University of Bonn, 53127 Bonn, Germany*

Edited by George M. Carman

**The nonlysosomal glucosylceramidase β2 (GBA2) catalyzes the hydrolysis of glucosylceramide to glucose and ceramide. Mutations in the human *GBA2* gene have been associated with hereditary spastic paraplegia (HSP), autosomal-recessive cerebellar ataxia (ARCA), and the Marinesco-Sjögren–like syndrome. However, the underlying molecular mechanisms are ill-defined. Here, using biochemistry, immunohistochemistry, structural modeling, and mouse genetics, we demonstrate that all but one of the spastic gait locus #46 (SPG46)-connected mutations cause a loss of GBA2 activity. We demonstrate that GBA2 proteins form oligomeric complexes and that protein–protein interactions are perturbed by some of these mutations. To study the pathogenesis of GBA2-related HSP and ARCA *in vivo*, we investigated GBA2-KO mice as a mammalian model system. However, these mice exhibited a high phenotypic variance and did not fully resemble the human phenotype, suggesting that mouse and human GBA2 differ in function. Whereas some GBA2-KO mice displayed a strong locomotor defect, others displayed only mild alterations of the gait pattern and no signs of cerebellar defects. On a cellular level, inhibition of GBA2 activity in isolated cerebellar neurons dramatically affected F-actin dynamics and reduced neurite outgrowth, which has been associated with the development of neurological disorders. Our results shed light on the molecular mechanism underlying the pathogenesis of GBA2-related HSP and ARCA and reveal species-specific differences in GBA2 function *in vivo*.**

The nonlysosomal β-glucosidase GBA2 resides as a membrane-associated protein at the cytoplasmic site of the endoplasmic reticulum and the Golgi, where it degrades the glycosphingolipid glucosylceramide (GlcCer)[5] to glucose and ceramide (1–3). GBA2 protein expression is highest in testis and brain tissue (2–4). In the testis, GBA2 seems to be mainly expressed in Sertoli cells, where it controls spermatogenesis and sperm-head shaping at the apical ectoplasmic specialization (4). Knocking out *Gba2* in mice results in a severe sperm morphological defect called globozoospermia (3, 4). This phenotype is caused by an accumulation of GlcCer, which changes the lipid composition of the membrane toward a more ordered state. In turn, cytoskeletal dynamics, in particular the F-actin

This work was supported by Deutsche Forschungsgemeinschaft (DFG) Grants SFB645 (to D. W. and P. D.), TRR83 (to D. W.), SPP1926 (to D. W.), SPP1726 (to D. W.), and FOR2743 (to D. W.), the Fritz-Thyssen Foundation (to D. W.), and the Boehringer Ingelheim Stiftung (to D. W.). The authors declare that they have no conflicts of interest with the contents of this article.

This article contains Figs. S1–S6 and Table S1.

[1] Both authors contributed equally to this work.

[2] Present address: Institute of Pharmaceutical Microbiology, University of Bonn, 53115 Bonn, Germany.

[3] Funded by the Deutsche Forschungsgemeinschaft (DFG, German Research Foundation) under Germany's Excellence Strategy – EXC2151 – 390873048.

[4] To whom correspondence should be addressed: Institute of Innate Immunity, University Hospital, University of Bonn, c/o Center of Advanced European Studies and Research (Caesar), Ludwig-Erhard-Allee 2, 53175 Bonn, Germany. Tel.: 49-228-9656-311; Fax: 49-228-9656-9311; E-mail: dwachten@uni-bonn.de.

[5] The abbreviations used are: GlcCer, glucosylceramide; HSP, hereditary spastic paraplegia; ARCA, autosomal-recessive cerebellar ataxia; FWHM, full-width at half-maximum; AHP, after-hyperpolarization potential; PFA, paraformaldehyde; aa, amino acid; DRM, detergent-resistant membrane; DAPI, 4′,6-diamidino-2-phenylindole; CV, column volume; BisTris, 2-[bis(2-hydroxyethyl)amino]-2-(hydroxymethyl)propane-1,3-diol; HBSS, Hanks' balanced salt solution; ICC, immunocytochemistry; DMEM, Dulbecco's modified Eagle's medium; FCS, fetal calf serum; WB, Western blotting; mPIC, mammalian protease inhibitor; DSS, disuccinimidyl suberate; CHO, Chinese hamster ovary; PDB, Protein Data Bank; GlcChol, glucosylcholesterol; PenStrep, penicillin/streptomycin; rsu, relative muscle strength unit; AP, action potential; GAPDH, glyceraldehyde-3-phosphate dehydrogenase; HexCer, hexosylceramide; rfu, relative fluorescence unit; MRM, multiple reaction monitoring; ANOVA, analysis of variance; Cer, ceramide; m, mouse; h, human; P, postnatal; NB-DNJ, *N*-butyldeoxynojirimycin; AMP-DNM, AMP-deoxynojirimycin; 4-MUG, 4-methylumbelliferyl-β-D-glucuronide hydrate; X-gal, 5-bromo-4-chloro-3-indolyl β-D-galactoside; ACSF, artificial cerebrospinal fluid.

organization at the ectoplasmic specialization, are dysregulated, and sperm-head shaping in the testis is disturbed (4). The male fertility defect was also observed when GBA2 activity was pharmacologically blocked *in vivo* in mice using the small molecular compound NB-DNJ (Miglustat) (5–7).

Although the enzyme has been identified more than 10 years ago, its physiological function in the brain is still enigmatic. GBA2 expression increases during neuronal differentiation (8). In the adult brain, GBA2 is predominantly expressed in neurons (2), with the highest expression level and activity in the cerebellum (9). In recent years, mutations in the *GBA2* gene (Spastic Gait locus #46 (SPG46), OMIM #614409) have been identified in patients with hereditary spastic paraplegia (HSP), autosomal-recessive cerebellar ataxia (ARCA), or the Marinesco-Sjögren–like syndrome (10–14). Patients are characterized by impaired gait and limb coordination in combination with cerebellar atrophy (15, 16).

The mutations found in the *GBA2* gene are either missense mutations, exchanging one amino acid for another, or nonsense mutations, leading to a premature transcriptional stop and thereby protein truncation (17). Most of the missense mutations are located in the C-terminal catalytic domain, and those leading to protein truncation lack the catalytic domain (17). The majority of SPG46 patients carry homozygous mutations and only a few are compound heterozygous mutant carriers (Table 1) (17). Some of the mutations have been analyzed *in vitro* and failed to produce a β-glucosidase activity (18). So far, only one mutation, R630W in the catalytic domain, has been functionally characterized *in vivo* (13). Leukocytes and lymphoblasts isolated from patients carrying the mutation in a homozygous state were devoid of GBA2 activity. Knocking down GBA2 expression in the zebrafish *in vivo* induced a curly tail and motility defects in some but not all fish (13). This phenotype was rescued by expressing hGBA2, but not by the hGBA2-R630W mutant (13). These results suggest that the mutations found in human patients result in a loss of GBA2 activity, thereby causing neurological defects and locomotor dysfunction. However, studies using GBA2-KO mice have not reported neurological or locomotion defects. Furthermore, it is not known how the different mutations affect GBA2 activity.

Here, we characterize the different mutations that were identified in SPG46 patients and demonstrate that all but one result in a complete loss of GBA2 activity. We provide the structural basis for the loss of function using structure–homology modeling and protein biochemistry. Furthermore, we demonstrate that the pharmacological block of GBA2 activity in cerebellar neurons diminishes neurite outgrowth. However, neurons isolated from GBA2-KO mice did not resemble this phenotype, although GBA2 activity was fully abolished. Behavioral studies analyzing locomotor function demonstrated a phenotypic variety in GBA2-KO animals. A few animals displayed a strong locomotor defect, but the majority of GBA2-KO mice showed only mild defects in the gait pattern, in contrast to what has been observed in human patients. Our results demonstrate the molecular mechanism underlying GBA2 function in neurons and reveal species-specific differences for GBA2 function *in vivo*.

## Results

### *Orthologous mutations in the mouse GBA2 gene cause a loss of activity*

Human and mouse GBA2 proteins share overall 87% sequence identity and 94% in the C-terminal catalytic domain. The 105-kDa GBA2 protein is composed of an N-terminal glucosyl-hydrolase family 116 domain of ~300 amino acid (aa) residues and a C-terminal catalytic domain, comprising aa 521–888 in humans (Fig. S2). Strikingly, the majority of amino acids mutated in human patients is identical in mouse and human GBA2, indicating that they are important for protein function. The different mutations are either missense or nonsense mutations (Figs. S1 and S2). Only the nonsense mutation Arg-870* in hGBA2 is not conserved and affects Gln-861* in mGBA2 (Figs. S1 and S2). The majority of missense mutations is localized in the C-terminal catalytic domain of GBA2, which is lacking in all nonsense mutants (Fig. S2). To characterize the effect of the mutations on GBA2 function, we introduced the different mutations into mGBA2 (Table 1) and characterized their expression and activity in CHO cells. All mutant mGBA2 proteins were expressed, as confirmed by Western blotting and immunocytochemistry (Fig. 1 and Fig. S3). The expression levels varied between mutants, and the deletion mutants migrated at a slightly higher molecular weight compared with the predicted molecular weight (Fig. 1 and Table 1), but none of the mutants showed a major difference in the subcellular localization compared with WT mGBA2 (Fig. S3). To analyze the activity of WT mGBA2 and the different mutants in CHO cells, we used a fluorescence-based activity assay (2). Apart from the variant mGBA2-R725H, all mutants were devoid of GBA2 activity (Fig. 1*B*) and only the mGBA2-R725H variant, which has been identified in a family with another disease-containing mutations, displayed a residual activity (Fig. 1*B*).

The first crystal structures of a member of the family of glycoside hydrolases have been recently determined (19, 20). This protein, designated GH116 β-glucosidase from *Thermoanaerobacterium xylanolyticum* (*Tx*), shares overall 32% sequence identity with hGBA2 and ~40% in the catalytic domain, with excellent correspondence between the active-site residues. All residues that bind the sugar moiety in *Tx*GH116 are conserved in hGBA2 (19). The homology to *Tx*GH116 allows modeling of human GBA2, based on PDB accession code 5BVU (20) using the workspace modeling approach of the Swiss-Model suite (21). The model of hGBA2 encompasses residues 77–888, with β-D-glucose as a ligand superimposed from the crystal structure 5BX5 (19). The protein adopts the two-domain architecture with an N-terminal β-sheet structure (aa 151–468) and the C-terminal all-helical catalytic domain (aa 473–888) (Fig. 1*C*). Two long α-helices combine the two domains (aa 441–490) with additional connecting loops of lower modeling confidence. These loops were suggested to participate in membrane interaction. The structure of *Tx*GH116 supports a peripheral membrane localization of GBA2, where it may bind to lipid headgroups or a transmembrane protein (19). The missense mutations D594H, R630W, G683R, R734H, and R873H all align to the catalytic domain of GBA2, whereas mutations F419V and M510V are located in the loop regions, connecting the two

**Table 1**
**Mutations in hGBA2 gene associated with locomotor dysfunction**

| Mutation | Alleles | Human GBA2 | Mouse GBA2 | Mass (mouse GBA2) | Associated disease | Refs. |
|---|---|---|---|---|---|---|
| | | | | *kDa* | | |
| **Missense** | | | | | | |
| 2618G→A | Homozygous | R873H | R864H | 103 | Autosomal-recessive cerebellar ataxia | 11 |
| 2201G→A | Homozygous (variant) | R734H | R725H | 103 | Autosomal-recessive cerebellar ataxia | 14 |
| 2048G→C | Homozygous | G683R | G674R | 103 | Hereditary spastic paraplegia | 10 |
| 1888C→T | Homozygous | R630W | R621W | 103 | Hereditary spastic paraplegia | 13 |
| 1780G→C | Homozygous | D594H | D585H | 103 | Autosomal-recessive cerebellar ataxia | 14 |
| 1528_1529del | Homozygous | M510V | M501V | 103 kDa | Marinesco-Sjögren-Like Syndrome | 12 |
| 1255T→G | Heterozygous, co-segregated with 2608C→T | F419V | F410V | 103 | Hereditary spastic paraplegia | 18 |
| **Nonsense** | | | | | | |
| 2608C→T | Heterozygous, co-segregated with 1255T→G | Arg-870* | Gln-861* | 97 | Hereditary spastic paraplegia | 18 |
| 1471_1474dupGGCA | Heterozygous, co-segregated with 518G→A | T492R*9 | T483R*9 | 55 | Hereditary spastic paraplegia | 13 |
| 1017C→T | Homozygous | Arg-340* | Arg-331* | 37 | Autosomal-recessive cerebellar ataxia | 11 |
| 700C→T | Homozygous | Arg-234* | Arg-225* | 26 | Hereditary spastic paraplegia | 13 |
| 518G→A | Heterozygous, co-segregated with 1471_1474dupGGCA | Trp-173* | Trp-164* | 18 | Hereditary spastic paraplegia | 13 |
| 363C→A | Homozygous | Tyr-121* | Tyr-112* | 12 | Autosomal-recessive cerebellar ataxia | 11 |

domains. Two residues are particularly involved in the coordination of the ligand. Based on the homologous structure of *Tx*GH116, Arg-873 makes a direct hydrogen bond to the 6-OH group of the glucosyl group (Fig. 1*D*, *inset*). Its mutation to histidine will abolish this hydrogen-bond formation due to the shorter side chain. Asp-594 forms a hydrogen bond to His-593, which coordinates the sugar moiety (Fig. 1*D*, *inset*). The D594H disease mutation might disrupt this paired side-chain coordination (19).

To get further insight into the structure–function relationship of mGBA2, we generated additional mutants that either lack the very C terminus adjacent to the catalytic domain or parts of the N terminus (Fig. S2). All of these mutants were expressed, but none of them displayed GBA2 activity (Fig. 1). This was particularly surprising for mGBA2-Q882*, which only lacks 36 amino acids at the C terminus, which are not necessary for the function of the nonmammalian glycoside hydrolase G116 family member *Tx*GH116. In summary, GBA2 only seems to be active as a full-length protein, requiring a precise 3D structure, whereas generation of a "minimal" GBA2 enzyme, comprising only the catalytic domain, seems impossible.

### *GBA2 proteins form oligomers*

Disease-associated mutations that are not localized in the catalytic domain might interfere with the structural integrity of the GBA2 protein, with protein–protein interactions, or protein association with membranes. Some members of other $\beta$-glucosidase families have been proposed to form dimers, which assemble as tetramers (22, 23). Thus, GBA2 might also form oligomeric complexes. To test this hypothesis, we first analyzed whether GBA2 interacts with itself by performing co-immunoprecipitation. Mouse GBA2-FLAG was heterologously expressed in CHO cells and purified using anti-FLAG magnetic beads. Co-transfection with mGBA2-HA demonstrated that, indeed, mGBA2-FLAG and mGBA2-HA interact (Fig. 2*A*), whereas unspecific binding to the anti-FLAG magnetic beads or interaction of an independent HA-tagged protein with mGBA2-FLAG was not observed (Fig. S4, *A* and *B*). To reveal the oligomeric state of the complex, we performed cross-linking experiments in CHO cells. Without cross-linking, mGBA2-FLAG migrated as a monomer in SDS-PAGE (~110 kDa), whereas after cross-linking, mGBA2-FLAG migrated as an oligomer (>245 kDa) (Fig. 2*B*). Next, we investigated whether mutations affect mGBA2 oligomerization. The missense mGBA2 mutants formed oligomeric complexes (Fig. 2*B*), whereas oligomer formation was dramatically reduced for some of the nonsense mutations (Fig. 2*C*). However, co-expression of WT and nonsense mutants did not result in hetero-oligomers, and the presence of the mutant did not affect oligomer formation of WT mGBA2 (Fig. 2, *C* and *D*). To investigate whether co-expression of mutant GBA2 with WT GBA2 affected the activity of the WT protein, we performed activity assays using WT and mutant mGBA2 proteins, co-expressed in CHO cells using a 2A peptide approach (Fig. 2, *E* and *F*). GBA2 activity in transfected cells was measured and normalized to the protein expression determined by Western blotting (Fig. 2, *E* and *F*). Compared with the WT-2A–WT control (set to 100%), the WT GBA2 activity in cells expressing WT-2A–mt accounts for 50% because only half the amount of WT GBA2 is expressed. If there is a dominant-negative effect, GBA2 activity in WT-2A–mt– expressing cells would account for significantly less than 50% activity compared with WT-2A–WT. However, a dominant-negative effect was not seen for any of the missense or nonsense mutants, because the activity in the WT-2A–mt conditions resembled an activity of about 50% (Fig. 2*F*). Only the R725H variant displayed ~80% activity in the WT-2A–mt condition (Fig. 2*F*), underlining that this mutant retains some GBA2 activity.

### *Loss of GBA2 leads to a defect in actin dynamics*

Our previous studies revealed that loss of GBA2 activity after pharmacological inhibition (NB-DNJ) or after loss of GBA2 (GBA2-KO) results in the accumulation of GlcCer, leading to a more ordered lipid organization in the plasma membrane. In turn, cytoskeletal dynamics, in particular actin dynamics, are disturbed, and the formation of lamellipodia is augmented (Fig. 3*A*) (4). To test whether re-expression of mGBA2 is sufficient to rescue the defects in the actin cytoskeleton, we overexpressed WT mGBA2-HA in fibroblasts from GBA2-KO mice (Fig. 3*B*). Indeed, mGBA2 expression reduced the lamellipodia count, demonstrating that expression of mGBA2 is sufficient to rescue the cytoskeletal defect (Fig. 3, *B* and *C*). Based on these results,

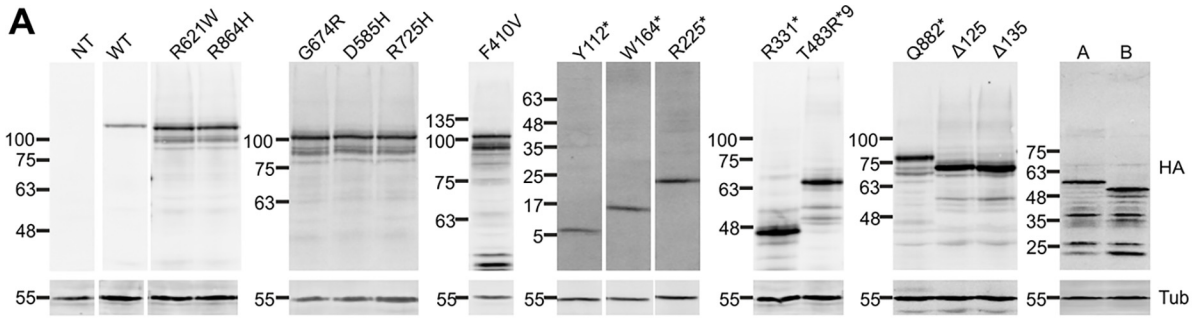


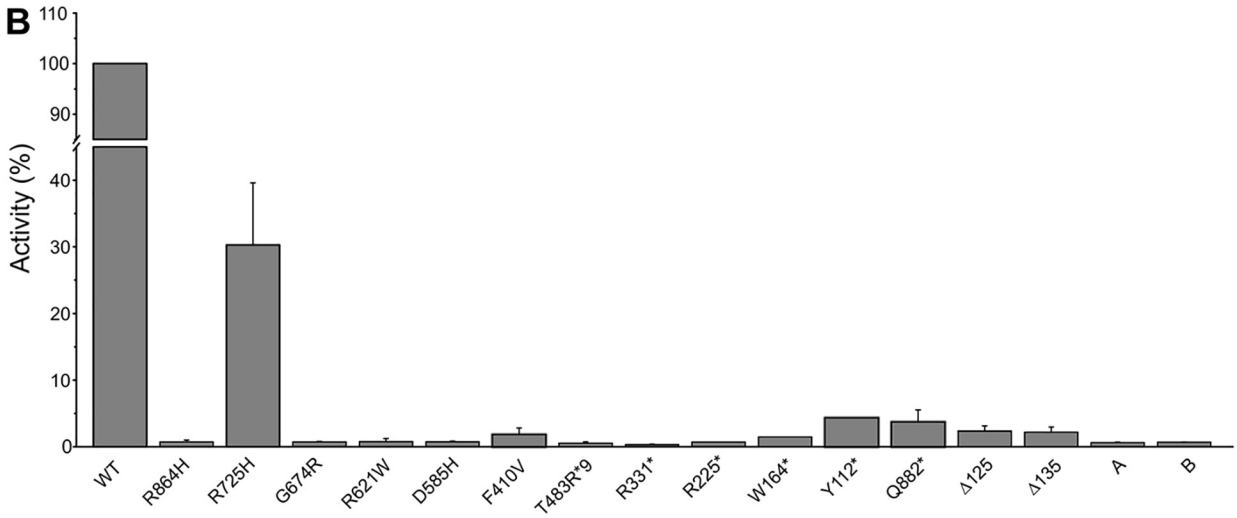


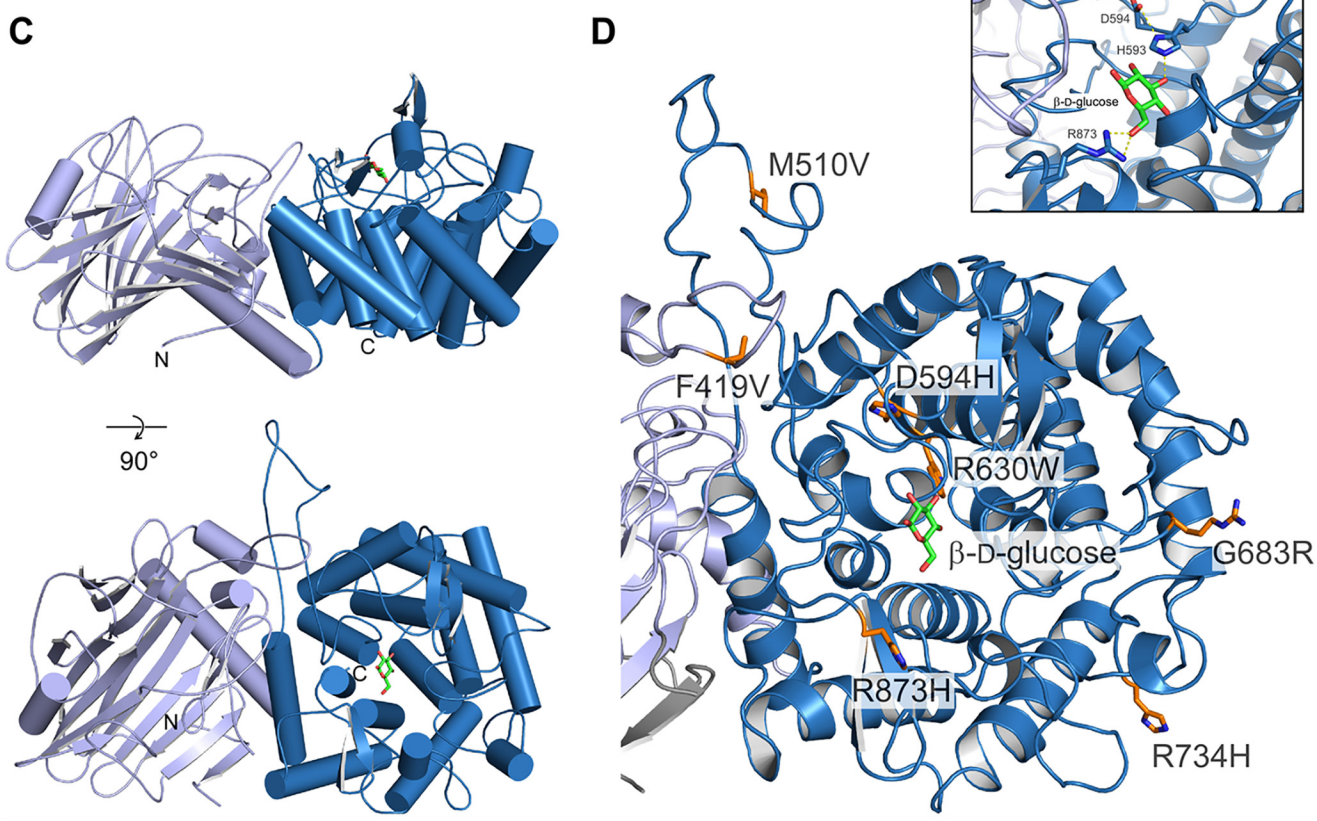

the mGBA2-R725H variant that retains GBA2 activity should also be able to rescue the cytoskeletal defects, whereas a mutant without GBA2 activity should fail to do so. To test this hypothesis, we expressed R725H and R621W in GBA2-KO fibroblasts (Fig. 3, *B* and *C*). In fact, mGBA2-R725H was also able to rescue the cytoskeletal defects (Fig. 3, *B* and *C*), whereas mGBA2-R621W–expressing fibroblasts were similar to GBA2-KO fibroblasts (Fig. 3*C*).

The Rho-GTPases Rac1 and Cdc42 are essential for lamellipodia and filopodia formation, respectively. The activity of Rac1, determined in a biochemical assay, was significantly increased in GBA2-KO compared with WT fibroblasts (Fig. 3, *D* and *E*), demonstrating that an increase in Rac1 activity underlies the increased number of lamellipodia in GBA2-KO fibroblasts. Thus, we treated GBA2-KO fibroblasts with a Rac1-specific inhibitor and analyzed lamellipodia formation. Treatment with the Rac1 inhibitor NCS23766 reduced lamellipodia numbers (Fig. 3*F*). To analyze whether the change in lipid order of the plasma membrane underlies the difference in Rac1 activity, we determined protein localization in detergent-resistant membranes (DRM) *versus* solubilized membranes. In GBA2-KO fibroblasts, Rac1 seemed to localize more in the DRM fraction compare with WT cells (Fig. 3*G*), indicating that the change in lipid order in GBA2-KO cells affects the localization and thereby the activity of Rho GTPases, in particular Rac1.

### *Loss of GBA2 activity diminishes neurite outgrowth*

The defect in actin dynamics in the absence of GBA2 was observed in every cell type analyzed in our studies. Thus, we wondered whether loss of GBA2 also affects cytoskeletal dynamics in neurons. We have previously shown that GBA2 is highly expressed in the brain, in particular in neurons (2). This is in line with findings using fluorescent activity-based probes, labeling active GBA2 in the spinal cord and different brain regions, predominantly in the cerebellar cortex (9). We further verified these results using global GBA2-KO mice and neuron-specific GBA2-KO mice (GBA2-KO$^{Syn}$). GBA2 expression was absent in brain, spinal cord, and cerebellum from GBA2-KO mice (Fig. 4*A*). In GBA2-KO$^{Syn}$ mice, GBA2 expression in brain and spinal cord was severely reduced (Fig. 4*B*), underlining the finding that GBA2 is predominantly expressed in neurons. The Eucomm GBA2-KO mouse model (GBA2-KO$^{Eu}$) expresses $\beta$-gal under the control of the GBA2 promotor, which allows visualizing GBA2 expression using X-gal staining. Labeling of spinal cord and brain sections as well as isolated cerebellar neurons nicely demonstrated GBA2 expression in neuronal cultures, in the gray matter of the spinal cord, and the cerebellum (Fig. 4, *C–E*). In line with the expression data, GBA2 activity was fully abolished in brain, spinal cord, cerebellum, and isolated cerebellar neurons from GBA2-KO mice (Fig. 4*F*).

Loss of GBA2 changes the glycosphingolipid homeostasis (3, 4, 24). To verify the changes in lipid homeostasis in the brain, in particular in the cerebellum, we analyzed the amount of neutral lipids in the cerebellum of P10 (postnatal day 10) and adult WT and GBA2-KO mice by MS, and we distinguished between sphingoid bases (long-chain bases, C18), ceramides (different chain length, saturated and unsaturated), and hexosylceramides (HexCer, different chain length, saturated and unsaturated). In the cerebellum of P10 mice, the total HexCer levels were not significantly different between genotypes; however, when comparing the chain lengths, HexCer-d18:1–18:0 levels were significantly increased in GBA2-KO compared with WT mice (Fig. S5, *A* and *B*). Similar results were obtained for the cerebellum of adult mice; total lipid levels remained unchanged in WT compared with GBA2-KO mice, but the levels of HexCer-d18:1–18:0 levels were significantly increased in GBA2-KO mice (Fig. S5, *C* and *D*). It has been shown before that the identity of the hexose sugar is glucose and not galactose (3) and that in GBA2-KO mice only GlcCer, but not GalCer, accumulates (26). None of the other neutral lipid species showed major differences between genotypes (Fig. S5, *A* and *C*). We also compared the levels of acidic lipids in the cerebellum of WT and GBA2-KO mice using TLC (Fig. S5, *E* and *F*). Levels of GM1a, GT1b, GD1b, and GM3 were all slightly increased in GBA2-KO compared with WT mice (Fig. S5*E*).

To reveal whether loss of GBA2 activity affects the cytoskeletal dynamics also in neurons, we isolated cerebellar neurons from P7 to P8 WT mice and treated them with the GBA2-specific blocker AMP-DNM for 48 h (27) (GBA2 activity control: 0.3 ± 0.1 rfu/min; 30 pM *N*-(5-adamantane-1-yl-methoxy-pentyl)-deoxynojirimycin (AMP-DNM): 0.03 ± 0.02 rfu/min; $n = 3$). Afterward, cells were fixed, and the F-actin and tubulin cytoskeleton were labeled. Strikingly, both NB-DNJ and AMP-DNM altered the cytoskeletal dynamics: more F-actin structures were formed, and the neurites appeared to be shorter (Fig. 4*G*). Quantification of the neurite length revealed that neurite length was significantly reduced in treated compared with non-treated samples (Fig. 4*H*). We performed the same experiments using cerebellar neurons from WT and GBA2-KO mice. However, although GBA2 activity was fully abolished (see Fig. 4*F*), neurite length was not different between genotypes (Fig. 4*H*).

To reveal whether the loss of GBA2 activity affects neuronal function, we performed electrophysiological recordings on isolated cerebellar neurons 48 h after dissection. We compared the

**Figure 1. Expression, activity, and structural modeling of GBA2.** *A,* heterologous expression of WT and mutant mGBA2 in CHO cells. Western blot analysis of hypotonic cell lysates was from nontransfected cells (*NT*), cells heterologously expressing WT mGBA2-HA (*WT*), or cells expressing different mGBA2 mutants. mGBA2 proteins were HA-tagged and labeled with an anti-HA antibody. Tubulin (*Tub*) was used as a loading control. 10–20 $\mu$g of protein were loaded per lane. *Lane A*, 6-hairpin glucosidase domain; *lane B*, glucosylceramidase domain. *B,* $\beta$-glucosidase activity in CHO cells. Cells were lysed in hypotonic buffer, and GBA2 activity was measured using the artificial, water-soluble substrate 4-methylumbelliferyl-$\beta$-D-glucopyranoside. *Columns* represent mean values of three independent experiments + S.D. (Arg-225*, Trp-164*, and Tyr-112* only $n = 1$). *Column A*, 6-hairpin glucosidase domain; *column B*, glucosylceramidase domain. *C,* structural modeling of hGBA2 based on the crystal structure of the bacterial $\beta$-glucosidase *T. xylanolyticum* *Tx*GH116. The N-terminal domain, formed by a two-sheet $\beta$-sheet sandwich (displayed in *light blue*), and the C-terminal all-helical catalytic domain (*dark blue*) are shown. *D,* display of the missense disease-associated mutations described for GBA2 in the structural model of the human isoform. Five mutations assemble in the catalytic domain, whereas F419V and M510V align to the linker region preceding the C-terminal domain. The mutations are shown in *stick* representations. The *inset* (*top right*) in *D* displays the hydrogen-bond interaction of Arg-873 with the glucose as well as the Asp-594–His-593 mediated interaction to the ligand.

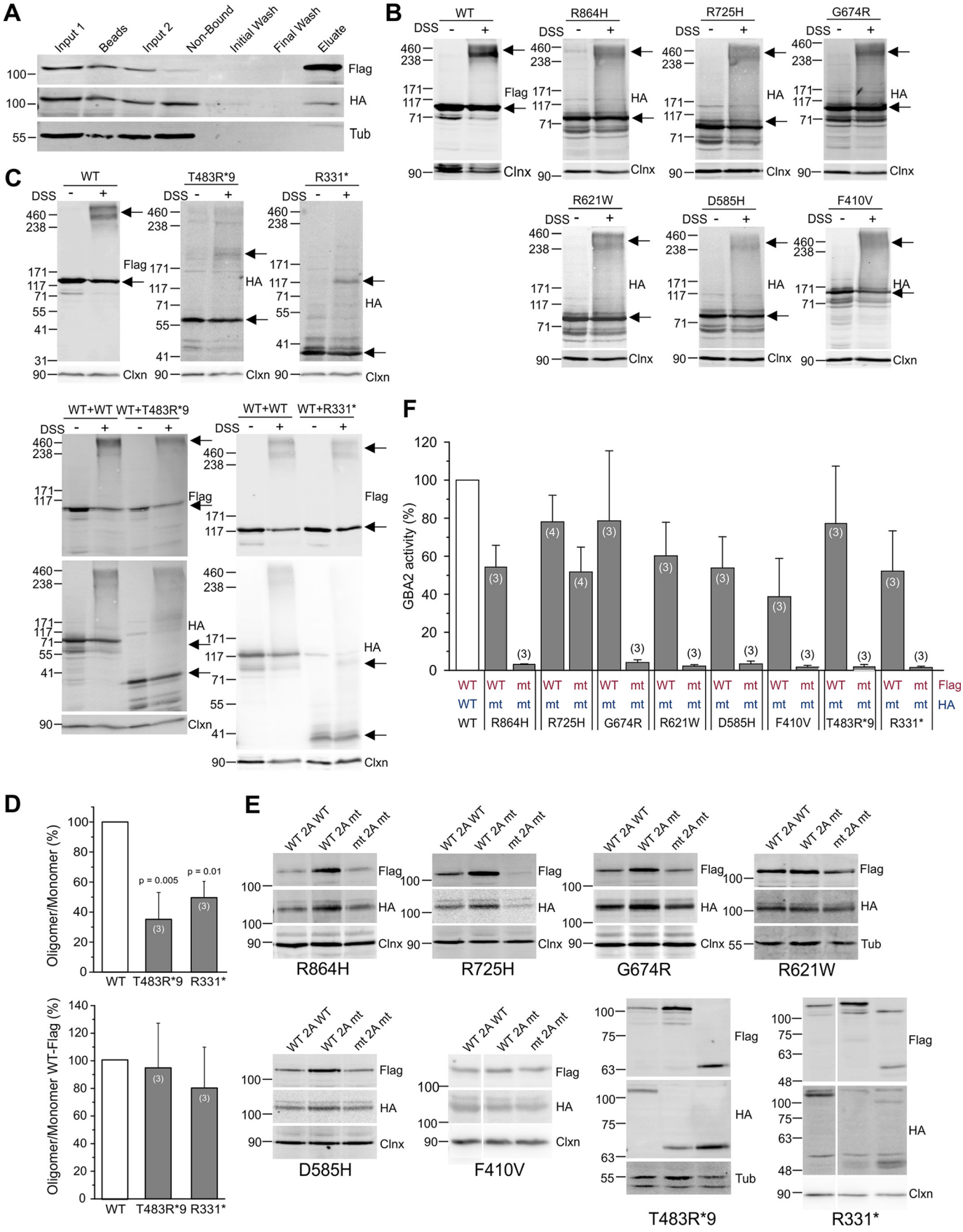

passive membrane properties, *i.e.* the resting membrane potential $V_{rest}$, the apparent input resistance $R_{in}$, and the membrane time constant $\tau_m$ between WT and GBA2-KO cells in the presence or absence of AMP-DNM (Table 2). All three parameters showed substantial variability, and no significant differences between the groups were detected. $R_{in}$ was remarkably high for all conditions, suggesting that under these conditions the neurons are equipped with few open ion channels. The presence of AMP-DNM slightly decreased $R_{in}$, which resulted in a significant difference between the WT and WT + 30 pM AMP-DNM group. As a consequence of the high $R_{in}$, $V_{rest}$ was highly variable between cells of all groups. GBA2-KO cells had slightly but statistically insignificant slower $\tau_m$.

### *Cerebellar morphology and neuronal function is not altered in GBA2-KO mice*

Patients suffering from HSP or ARCA display, among other defects in the central nervous system, cerebellar atrophy. Thus, we analyzed whether GBA2-KO mice also show brain morphological defects. The brain weight of age- and sex-matched WT and GBA2-KO mice was not different, and gross brain morphology remained unchanged (WT: 440 ± 16 mg ($n$ = 10) *versus* KO: 435 ± 18 mg ($n$ = 17), see Fig. 5*A*). Histological analyses of brain cryosections from P18 or adult WT and GBA2-KO mice did not show any abnormalities in gross lobular morphology. Moreover, no Purkinje cell degeneration, resulting in loss or reduced cell numbers in the Purkinje cell layer, was observed (Fig. 5, *B* and *C*).

To test whether loss of GBA2 affects the function of Purkinje cells within their neuronal network, we performed electrophysiological recordings on acute cerebellar slices. We compared passive and active properties (*i.e.* properties of action potentials) of Purkinje cells between WT and GBA2-KO mice (Fig. 5, *D–F*). Similar to the passive properties of isolated cerebellar neurons, the passive properties of Purkinje cells had a high cell-to-cell variability, and no differences between WT and GBA2-KO mice were detected. Purkinje cells of GBA2-KO mice tended to have a slightly lower $R_{in}$ (Tables 2 and 3). The active properties of Purkinje cells did not significantly differ between WT and GBA2-KO mice (Table 3). After recording, slices were fixed in 4% PFA for 30 min, and the morphologies of the recorded and Alexa Fluor 488-filled Purkinje cells were compared. However, no major differences in Purkinje cell morphology between WT and GBA2-KO cells were observed (Fig. 5*G*).

### *Loss of GBA2 alters the gait pattern*

To reveal whether GBA2-KO mice show a defect in muscle strength or locomotion, similar to human SPG46 patients, we performed different behavioral assays. The weight test allows measuring the muscle strength of the front paws, whereas the CatWalk gait analysis allows determining static and dynamic locomotion parameters. Of note, GBA2-KO mice showed a higher tendency to develop seizures: four global GBA2-KO mice above the age of 30 weeks suffered from seizures, which were never observed in age-matched WT mice. The weight test revealed that the muscle strength of the front paws was reduced in GBA2-KO compared with WT mice (Fig. 5*H*). Using the CatWalk analysis, we first observed that two GBA2-KO mice were barely moving and exhibited a wide-based gait in their hind paws, excluding them from further analysis. In contrast, none of the WT mice showed this strong locomotion defect. Apart from these two mice, the differences between WT and GBA2-KO mice in the CatWalk were rather mild. To stabilize their gait, mice suffering from motor coordination defects often exhibit a shortened duration of the front paws' swing phase, which refers to the time when a paw is lifted and not in contact with the glass plate. However, this parameter was not different between WT and GBA2-KO mice (Fig. 5, *I* and *J*). To determine the interpaw coordination, phase dispersion was measured. This parameter describes the temporal relationship between the different paw placements by taking into account the phase lag of the paws. Values for interpaw coordination of the diagonal, ipsilateral, and girdle paw pairs showed a higher variation in GBA2-KO compared with WT mice, but there was no significant difference for either paw combination (Fig. 5*K*). Next, we analyzed the step sequence. In general, quadrupedal animals use six patterns of step sequence, the most commonly observed pattern in mice being the alternate AB pattern (Fig. 5*L*) (28). Indeed, both WT and GBA2-KO mice predominantly used the AB pattern (Fig. 5*M*). However, the frequency of AB pattern appearance was reduced in GBA2-KO compared with WT mice (Fig. 5*M*). Instead, GBA2-KO mice more frequently used the AA, CB, and CA pattern (Fig. 5*M*), demonstrating that the

**Figure 2. Oligomerization and activity of mGBA2.** *A,* co-immunoprecipitation of mGBA2-HA with mGBA2-FLAG using anti-FLAG magnetic beads (FLAG-Trap) after pre-clearing on underivatized agarose beads. 250 μg of total protein was loaded in a total volume of 500 μl on equilibrated agarose (50 μl of bead slurry of a 50% suspension in storage buffer was used) and incubated at 4 °C. After pre-clearing, supernatant was incubated on anti-FLAG magnetic beads (50 μl of bead slurry of a 50% suspension in storage buffer was used) overnight at 4 °C. *Input,* 16.67 μl of protein lysate before (*Input 1*) or after (*Input 2*) pre-clearing. *Beads*, 25 μl of agarose matrix resuspended in 30 μl 1× SDS sample buffer. *NonBound*, 37.5 μl of supernatant after incubation of the lysate on the beads. *Initial* and *Final Wash*, 37.5 μl of supernatant after washing the beads with 300 μl of washing buffer. *Eluate*, 37.5 μl of supernatant was loaded after elution in 100 μl of 1 M glycine, pH 3.0, and neutralization in 16.67 μl of 1 M Tris/HCl, pH 8.0. GBA2-FLAG and mGBA2-HA were detected using FLAG- or HA-specific antibodies, respectively. β-Tubulin (*Tub*) was used as a loading control. *B,* chemical cross-linking of WT and mutant mGBA2. Western blot analysis of WT mGBA2-FLAG and missense mGBA2 mutants (all HA-tagged) expressed in CHO cells before (−) and after cross-linking with 0.77 mM DSS (+) under hypotonic buffer conditions. mGBA2-FLAG and mGBA2-HA were detected using FLAG- or HA-specific antibodies. 40 μg of total protein was subjected to chemical cross-links and loaded per lane. Calnexin (*Clnx*) served as a loading control. *C, top,* see *B* for nonsense mutants. *Bottom,* chemical cross-linking of WT mGBA2-FLAG in the presence of WT mGBA2-HA or nonsense mGBA2-HA. Cross-linking conditions and Western blot analysis was performed similar to *B*. *D,* quantitative analysis of *C*. *Top,* oligomer/monomer ratio of mutant mGBA2-HA compared with WT mGBA2-FLAG (set to 100%). *Bottom*, oligomer/monomer ratio of mGBA2-FLAG in the presence of WT mGBA2-HA (set to 100%) or nonsense mGBA2-HA. *E,* expression of the mGBA2 2A-peptide constructs designed for the stoichiometric expression of FLAG- and HA-tagged mGBA2. Western blot analysis of GBA2 expression in transfected CHO cells expressing either mGBA2-FLAG and mGBA2-HA (*WT 2A WT*), mGBA2-FLAG and mutant mGBA2-HA (*WT 2A mt*), or mutant mGBA2-FLAG and mutant mGBA2-HA (*mt 2A mt*). mGBA2-FLAG and mGBA2-HA were detected using FLAG- or HA-specific antibodies. 20 μg of protein was loaded per lane. Calnexin or β-tubulin served as a loading control. *F,* β-glucosidase activity in CHO cells expressing mGBA2-2A constructs as depicted in *E*. Cells were lysed in hypotonic buffer, and GBA2 activity was measured using the artificial, water-soluble substrate 4-methylumbelliferyl-β-D-glucopyranoside. *D* and *F,* columns represent mean values of three independent experiments + S.D. *n* indicates numbers, and *p* values calculated using one-way ANOVA are indicated.

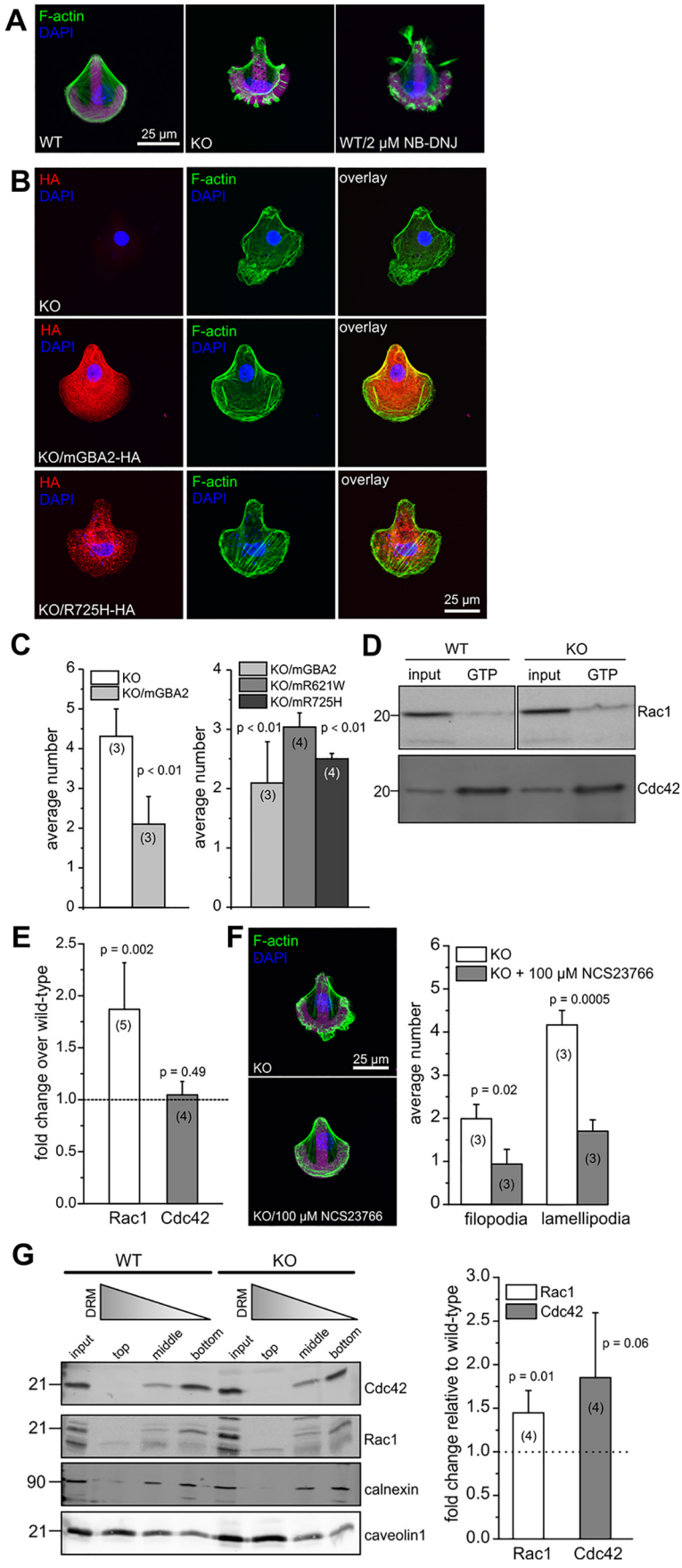

step sequence in GBA2-KO mice is more variable and unstable compared with WT mice.

## Discussion

Mutations in the *GBA2* gene have been identified in human patients, who suffer from a combination of spastic paraplegia and cerebellar ataxia. Our results reveal that all but one mutation of these SPG46-connected mutations cause a loss of GBA2 activity. Because most of the affected patients are homozygous carriers, patients most likely are devoid of GBA2 activity. This is particularly true for a recently identified homozygous mutation in the *hGBA2* gene, which resides in the splice acceptor site of exon 3 and results in a complete loss of mRNA expression (29). Thus, GBA2-KO mice should serve as a mammalian model system to study the molecular mechanism that links the loss of GBA2 activity with the development of locomotor dysfunction. However, our results demonstrate that GBA2-KO mice do not fully resemble the human phenotype. The phenotype in GBA2-KO mice is variable, with some mice showing a strong defect in locomotion, whereas others only display a mild defect in the gait pattern. This phenotype variation could be due to a reduced penetrance, resulting from difference in age, sex, or strain background. The latter has been shown to have severe consequences on the GBA2-associated phenotypes, *i.e.* male infertility. The administration of low doses of NB-DNJ to inbred strains of the C57 lineage produced high percentages of abnormal sperm that lack an acrosome, whereas mouse strains like BALB/c show intermediate percentages, and most strains from the Swiss and Castle lineages do not show a major defect in sperm morphology (30). In this respect, it is striking that miglustat (NB-DNJ), which is used in the clinics for the treatment of Gaucher disease because it blocks the glucosylceramide synthase, but also GBA2 at a higher potency, does not cause male infertility in humans (31). As described above, in mice, miglustat treatment results in male infertility only in some genetic backgrounds (5, 6, 31). In human patients, one affected male patient (homozygous for Tyr-121*) produced offspring (11), whereas two other affected male patients (homozygous for R630W and compound heterozygous for T492R*9/W173*9) were infertile and showed bilateral testicular hypertrophy with sperm-head defects (13). Thus, the genotype does not allow us to predict the phenotypic outcome with respect to male fertility, and there seems to be species-specific differences for GBA2 function *in vivo*.

The same might be true for defects in locomotor function. None of the patients receiving miglustat treatment reported locomotor dysfunction (32–34). Furthermore, human patients carrying mutations in the *GBA2* gene also show a variety in phenotype, including differences in peripheral neuropathy and in the onset of the disease. However, all homozygous carriers of the mutations display an ataxic phenotype. In the mouse model, the variation in phenotype could be due to a difference in the genetic background. But this cannot be the case for the difference in locomotor dysfunction in GBA2-KO mice because the animals were all kept at the same genetic background. In other HSP mouse models, defects in locomotion occur later in life in mice compared with humans (35, 36). However, GBA2-KO mice were analyzed between 30 and 34 weeks of age at a time point, where other HSP models already displayed a defect in locomotion.

Another explanation for the phenotypic variance of GBA2-KO mice could be that individual mice accumulate different amounts of GlcCer. Such a correlation between the level of accumulated glycosphingolipid and the severity of the phenotype is seen in human patients suffering from Fabry disease. Mutations in the *GLA* gene, encoding for the $\alpha$-galactosidase A, leading to complete or partial loss of the enzyme's activity, result in a moderate or severe accumulation of Gb3 and in a moderate or severe form of the disease, respectively. Serum levels of deacylated Gb3 in blood plasma was the highest in patients suffering from the classic, severe form of the disease, whereas the lowest plasma deacylated Gb3 levels were present in patients suffering from the late-onset, milder form of the disease (37). Thus, not only a genotype–phenotype correlation, but also a genotype–lipidome–phenotype correlation might be useful for further *in vivo* studies. This approach would also be important to disentangle the role of GlcCer and the accumulation of higher order glycosphingolipids in the brain (see Fig. S5, *E* and *F*). A difference in lipid accumulation between different GBA2-KO could also explain the occurrence of seizures in some, but not all GBA2-KO.

In HSP mouse models, defects in axonal branching were identified as a common denominator, which might underlie disease progression (35, 36). Sphingolipid synthesis has shown to be crucial for neuronal outgrowth. In cells treated with an inhibitor for ceramide synthase (fumonisin B1), axon growth was impaired at stage 3 during neuronal development after 2–3

**Figure 3. Alterations in Rho GTPase activity and localization underlie the cellular defects in GBA2-KO fibroblasts.** *A,* actin defects in fibroblasts lacking GBA2 activity. Fluorescent labeling of F-actin in wildtype (*WT*), GBA2-KO (*KO*), and WT fibroblasts treated with 2 $\mu$M NB-DNJ (WT/2 $\mu$M NB-DNJ). Cells were seeded on CYTOO chips with cross-bow micro-patterns that are coated with fluorescently-labeled fibronectin (*purple*). F-actin was stained with Alexa Fluor 488 phalloidin (*green*) and the DNA with DAPI (*blue*). *Scale bar* is indicated. *B,* heterologous expression of WT mGBA2 and mGBA2 mutants in GBA2 KO-fibroblasts. See *A* for GBA2-KO fibroblasts (*KO*) expressing WT mGBA2-HA (*KO/mGBA2-HA*), and mGBA2-R725H-HA (*KO/R725H-HA*). mGBA2 proteins were HA-tagged and expression was detected with an anti-HA antibody (*red*). *C,* quantification of actin cytoskeletal structures. Average numbers of lamellipodia were determined in GBA2-KO fibroblasts (*KO*) and in GBA2-KO fibroblasts heterologously expressing WT mGBA2-HA (*KO/mGBA2-HA*), mGBA2-R725H-HA (*KO/R725H-HA*), and mGBA2-R621W-HA (*KO/R621W-HA*). *D,* activity of Rho GTPases in GBA2-KO fibroblasts. Active GTP-bound Rac1 and Cdc42 from wildtype (*WT*) and GBA2-KO fibroblast (*KO*) lysates were affinity-purified using PAK-GST and analyzed by Western blotting; 10 $\mu$g of the cell lysate was used as input. The blot was probed with a Rac1- and a Cdc42-specific antibodies. *E,* quantification of activated Rac1 and Cdc42 in GBA2-KO fibroblasts. Rac1-GTP and Cdc42-GTP expression was normalized to the input and expressed as fold change over WT levels. *F,* Rac1 inhibition in GBA2-KO fibroblasts. *Left,* fluorescent labeling of F-actin in GBA2-KO (*KO*) fibroblasts treated with 100 $\mu$M NCS23766 (*KO/100 $\mu$M NCS23766*). Cells were seeded on CYTOO chips with cross-bow micro-patterns that are coated with fluorescently-labeled fibronectin (*purple*). F-actin was stained using Alexa Fluor 488 phalloidin (*green*), and the DNA was stained with DAPI (*blue*). *Scale bar* is indicated. *Right,* average numbers of cytoskeletal structures were determined. *G,* expression of Rho GTPases at DRM. *Left,* DRM were isolated from wildtype (*WT*) and GBA2-KO (*KO*) fibroblast lysates in a gradient. *Top, middle,* and *bottom fractions* were analyzed by Western blotting and probed with Rac1- and Cdc42-specific antibodies. Caveolin1 and calnexin were used as markers for DRM-associated and non-DRM associated proteins, respectively. The distribution of DRM is represented in *gray*. *Right,* Rac1 and Cdc42 expression in the middle fraction was normalized to the input and represented as fold change over WT levels. All data are presented as mean ± S.D.; *n* indicates numbers, and *p* values were calculated using one-way ANOVA are indicated.

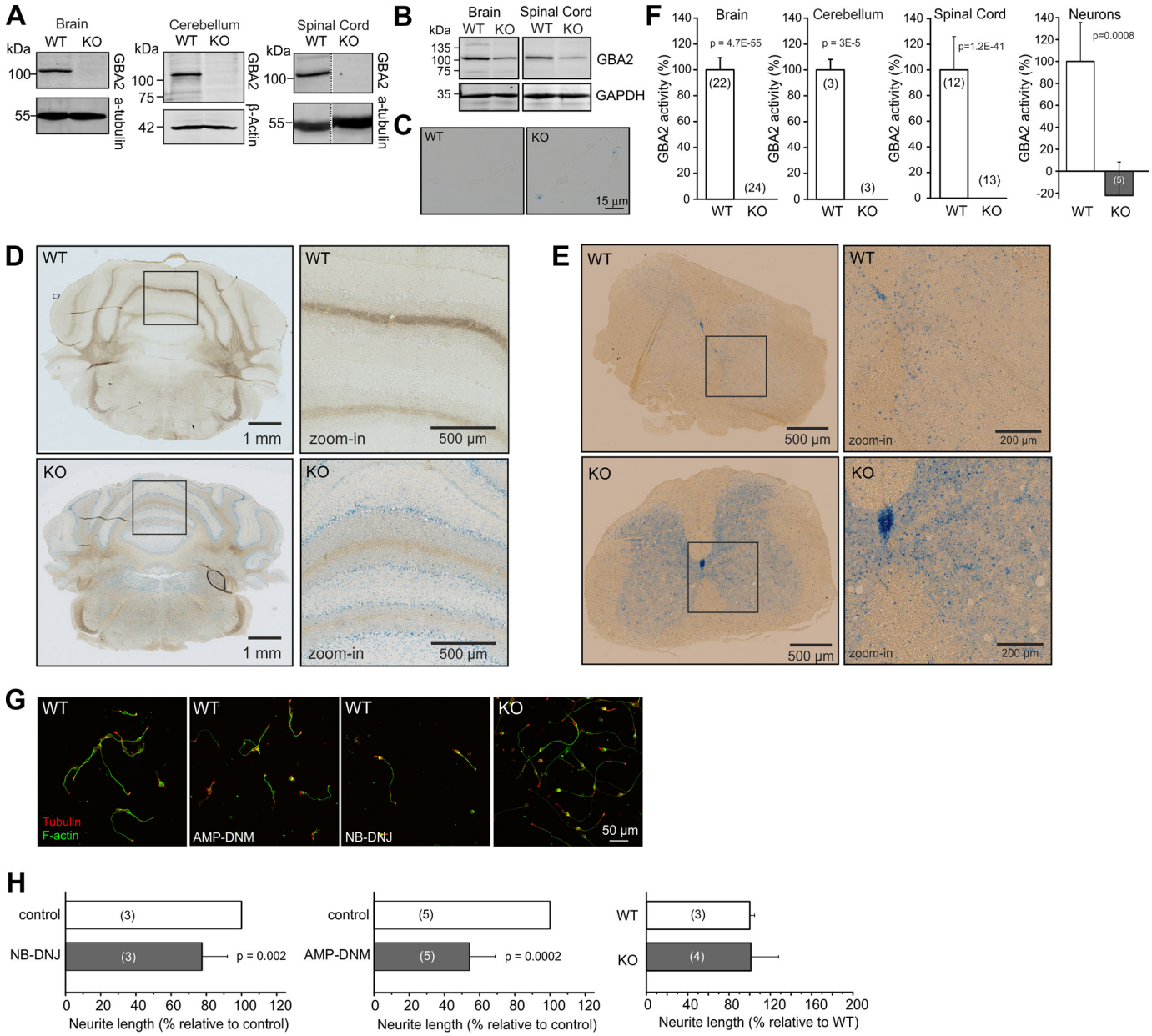


**Figure 4. Loss of GBA2 activity reduces neurite outgrowth.** *A,* GBA2 expression in brain (adult), spinal cord (adult), and cerebellum (P8) from wildtype (*WT*) and GBA2-KO (*KO*; $KO^{Eu}$) mice. Hypotonic protein lysates were subjected to Western blot analysis, and the membrane was labeled with an anti-GBA2 antibody; α-tubulin was used as a loading control. *B,* GBA2 expression in brain and spinal cord from adult WT and neuron-specific GBA2-$KO^{syn}$ mice. Hypotonic protein lysates were subjected to Western blot analysis, and the membrane was labeled with an anti-GBA2 antibody. GAPDH was used as a loading control. 60 μg of hypotonic protein lysates were loaded per lane. *C,* β-gal expression in cerebellar neurons. Cerebellar neurons were isolated from P9 WT and GBA2-$KO^{Eu}$ mice and labeled with X-gal. *D,* β-gal expression (*blue*) in the brain of adult wildtype (*WT*) and GBA2-$KO^{Eu}$ (*KO*) mice. Pictures on the *right* show a *zoom-in* of the cerebellar region indicated with a *box* on the *left*. *E,* see *D* for spinal cord. Pictures on the *right* show a *zoom-in* of the region indicated with a *box* on the *left*. *F,* GBA2 activity in hypotonic lysates from adult brain (35 ± 9 weeks), cerebellum (P8), adult spinal cord (45 ± 12 weeks), and isolated cerebellar neurons (P8–9) from WT and GBA2-KO/GBA2-$KO^{Eu}$ mice. *G,* neurite outgrowth of cerebellar neurons (P6–9). Representative images of WT cells treated with 30 pM AMP-DNM or 5 μM NB-DNJ for 48 h, or GBA2-KO cells, fixed, and stained with an anti-tubulin antibody (*red*) and rhodamine-conjugated phalloidin (*green*) to measure neurite outgrowth. *H,* quantification of the neurite length of cells presented in *G*. *N* numbers and *p* values in *F* and *H* were calculated using one-sample Student's *t* test.

days in culture (38). This was also shown for dendritic growth in Purkinje cells upon ceramide synthase inhibition (39). Impaired *de novo* synthesis of ceramide resulted in decreased ganglioside levels (38, 39). It is not the lack of ceramide itself but rather of its glycosylated metabolite GlcCer, as the glycosphingolipid precursor, that underlies this axon outgrowth defect. In the presence of fumonisin B1, it was a ceramide derivative, which is glycosylated to GlcCer, that ameliorated the axon outgrowth defect, whereas a ceramide derivative, which cannot be glycosylated to GlcCer, failed to do so (38–40). Similarly, the oligosaccharide $II^3$ NeuAc-$Gg_4$ rather than the ceramide part of the GM1 ganglioside promotes neurite formation in neuroblastoma cells (41). Also, inhibition of GBA2-mediated degradation of GlcCer affected neurite outgrowth.: Pharmacological inhibition of GBA2 activity by NB-DNJ in cerebellar neurons resulted in significantly shorter neurites (see Fig. 4). GBA2 expression

**Table 2**

**Passive properties of cultured cerebellar cells recorded 48 h after preparation**

A current step protocol was used to determine passive properties of cerebellar cells recorded in the whole-cell current-clamp configuration. Mean age of mice at day of dissection was 10.6 ± 0.5 days. WT $n = 9$; WT + 30 pM AMP-DNM; $n = 10$, KO $n = 8$, KO + 30 pM AMP-DNM, $n = 5$. The Student's $t$ test was used to test statistical significance between indicated groups.

| | WT, mean ± S.D. | WT + inhibitor, mean ± S.D. | KO, mean ± S.D. | KO + inhibitor, mean ± S.D. | $p$, WT *vs.* KO | $p$, WT *vs.* WT + inhibitor |
|---|---|---|---|---|---|---|
| $V_{rest}$ | −75 ± 23 | −61 ± 16 | −69 ± 18 | −65.3 ± 5.8 | 0.58 | 0.17 |
| $\tau_m$ (ms) | 24.9 ± 8.3 | 25.8 ± 9.4 | 28.9 ± 8.5 | 25.7 ± 6.3 | 0.34 | 0.84 |
| $R_{in}$ (gigaohm) | 7.6 ± 2.6 | 4.9 ± 1.3 | 7.2 ± 2.2 | 5.9 ± 0.6 | 0.73 | 0.017 |

increases during neuronal differentiation (8), implicating that the enzyme plays a pivotal role in the CNS already during development.

Axon branching crucially relies on F-actin dynamics (42–44), which are controlled by Rho GTPases (45). Loss of GBA2 results in the accumulation of GlcCer, which changes the lipid composition of the membrane toward a more ordered state (4). Our results demonstrate that the Rho GTPases Cdc42 and Rac1 are sensitive to these alterations in the lipid environment of the plasma membrane, which changes their localization and activity. In all cell types we have analyzed so far, the loss of GBA2 and the consequent accumulation of GlcCer led to a dramatic change in the F-actin cytoskeleton. We also observed cytoskeletal defects in isolated cerebellar neurons when acutely blocking GBA2 activity, leading to a reduction in neurite outgrowth and the formation of extra F-actin structures. This includes *GBA2* in the list of genes, which are mutated in HSP patients and whose loss of function results in alteration of neurite formation and axonal branching. However, this cellular phenotype was only observed when GBA2 activity was pharmacologically blocked and not when GBA2 was genetically ablated. Isolated cerebellar neurons from GBA2-KO mice were morphologically indistinguishable from WT neurons, although GBA2 activity was fully absent. This might explain why GBA2-KO mice predominantly show a mild phenotype, which does not resemble the human phenotype. The molecular mechanisms underlying this phenotype discrepancy are enigmatic.

In the context of Gaucher disease, a lysosomal storage disorder that develops due to loss of GBA1 activity, we have demonstrated that loss of GBA1 activity results in a concomitant reduction in GBA2 activity (24). However, vice versa, loss of GBA2 activity does not affect GBA1 activity (24). In fact, we also did not observe a change in GBA1 activity in the brain or neurons from GBA2-KO mice (Fig. S6). The GBA activity assay bears one major shortcoming by using the water-soluble 4-MUG and not GlcCer as a substrate. However, we have extensively characterized our assay to verify that it reliably distinguishes GBA1 and GBA2 activity (2). Thus, the difference in phenotype cannot be explained by compensation through an increase in GBA1 activity. Another way of determining GBA2 activity would be to use activity-based probes, which can be used on live cells and brain sections (9, 47). Whether also other risk factors contribute to disease progression in SPG46 patients remains unknown.

Of note, GBA2 also exerts a transglucosylation activity and can transfer a glucose moiety from GlcCer to cholesterol or, vice versa, deglycosylate glucosylcholesterol (GlcChol), transferring the glucose moiety to ceramide (48, 49). GlcChol is abundant in the brain, sciatic nerve, and lung (49). Loss of GBA2 is accompanied by a decrease in GlcChol levels, as observed in thymus, liver, and blood plasma (49), in murine dermal fibroblasts, testis, and also in the brain (testis: WT, 1.5 ± 0.3, *versus* KO, 1.1 ± 0.2 pmol/mg protein; fibroblasts: WT, 14.3 ± 3.1, *versus* KO, 2.1 ± 0.3 pmol/mg protein; brain: WT, 2.0 ± 0.2, *versus* KO: 0.3 ± 0.1 nmol/g; mean ± S.D., $p < 0.05$ for all samples). Upon glycosylation, cholesterol relocalizes from ordered to less ordered membrane domains (50). Thus, not only is GlcCer and GlcChol metabolism strongly linked, but also the function of these lipid metabolites might be intertwined on the level of lipid rafts. In a GBA2-deficient condition, in which glycosylation of cholesterol is diminished, cholesterol might still localize to more ordered membrane domains, promoting the effect of accumulated GlcCer on membrane stacking. However, the cellular function of GlcChol is still unclear. Because GlcChol is more water-soluble than cholesterol, a potential role of GlcChol as an ATP-independent transport metabolite of cholesterol was suggested (49). Interestingly, a glycosylated sterol (sitosterol) from cycads was shown to be toxic to neurons *in vivo* in mice and *in vitro* (51). However, whether GlcChol in mammals also exerts a neurotoxic function and whether a decrease in GlcChol ameliorates neuronal damage need to be elucidated.

In summary, GBA2 seems to fulfill cell-type and species-specific functions and the molecular mechanisms underlying these differences need to be carefully studied in future experiments. This will allow the shedding of light on the physiological role of GlcCer-dependent signaling pathways and the understanding of molecular mechanisms underlying GlcCer storage diseases in humans.

## Materials and methods

### Cloning

The ORF of mouse GBA2 (NM_172692) was amplified from cDNA using primers containing restriction sites and a Kozak sequence in front of the start codon. The sequence encoding a hemagglutinin (HA) or FLAG tag was added by PCR at the 3′-end. PCR products were subcloned into pcDNA3.1(+) or pcDNA6/V5-HisA, and their sequence was verified. These mGBA2 constructs were used as a template to generate double chimera, including a FLAG-tagged mGBA2 and a coding sequence for the 2A peptide (VKQTLNFDLLKLAGDVESNPGP) at the N terminus and an HA-tagged mGBA2 at the C terminus. Addition of the 2A peptide flanked by a PPGSG- and GSG-linker to the FLAG-tagged mGBA2 was performed in a sequential manner. The final chimeric prod-

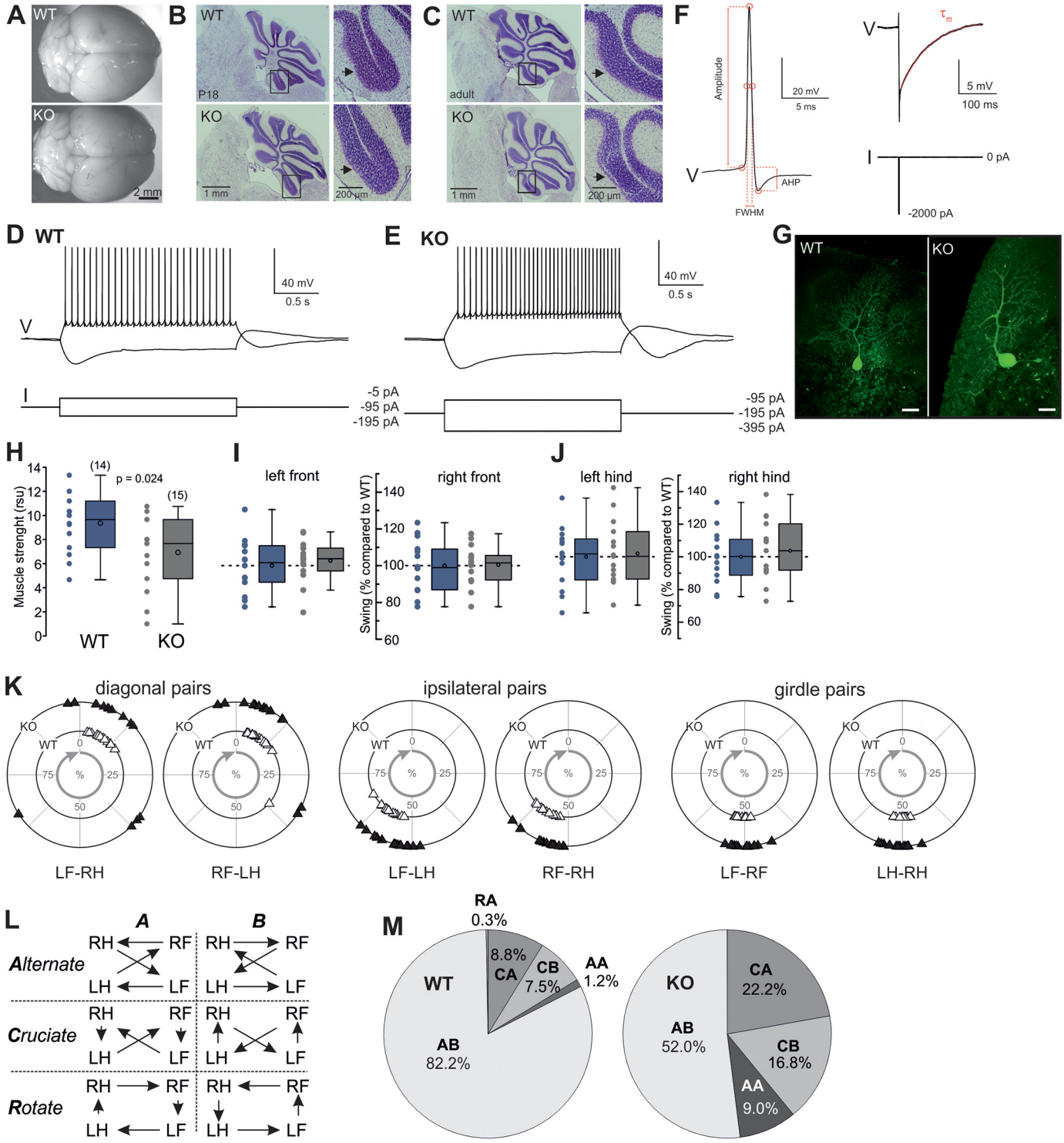


**Figure 5. GBA2-KO mice exhibit gait abnormalities.** *A,* brain of wildtype (*WT*) and GBA2-KO (KO$^{Eu}$ (*KO*)) mice. *B,* Nissl staining of sagittal sections from P18 WT and GBA2-KO mice. *C,* see *B* for adult mice. *D* and *E,* whole-cell current-clamp recordings of a WT (*D*) and GBA2-KO (*E*) Purkinje cell in an acute cerebellar slice responding to different current steps. *F, left,* exemplary AP of a WT Purkinje cell, indicating how active AP parameters (amplitude, FWHM, and AHP) were determined. *Right,* exemplary voltage response of a WT Purkinje cell to a −2000 pA injection and monoexponential fit to determine $\tau_m$. *G,* Purkinje neurons of WT and GBA2-KO mice, filled with Alexa Fluor 488 (*green*) after patch-clamp experiments. *Scale bar,* 20 $\mu$m. *H,* weight test. Muscle strength (rsu) of the front paws was calculated for adult (30 ± 2 weeks) WT and GBA2-KO mice. *Box plot* includes the 25th and 75th percentile (*top* and *bottom boundaries*), median (*horizontal line*), average (*circle in box*), minimum and maximum (*whisker boundaries*); individual data points are plotted aside. *I–M,* gait analysis using the CatWalk system of adult (32 ± 2 weeks) WT and GBA2-KO mice. *I,* swing duration of front paws. The swing phase for each paw was calculated and normalized to the mean duration of the swing phase for the corresponding WT paw (set at 100%, indicated with a *dotted line*). *Box plot*: see *H*; (*WT*: $n = 14$, *KO*: $n = 15$). *J,* see *I* for hind paws. *K,* interlimb coordination. Circular scatter plot representing the phase dispersion, taking into account the phase lag of the paws for the diagonal, the ipsilateral, and the girdle pairs between WT and GBA2-KO mice, and ranges from 0 to 100%. *L,* step patterns to determine inter-limb coupled movements are sorted in six different patterns. *M,* distribution of regular step patterns in WT (*left*) and GBA2-KO (*right*) mice (WT: $n = 14$, KO = 15) presented as $\pi$ graphs, showing the relative frequency of each pattern (*AA,* WT *versus* KO, $p = 0.015$; *AB,* WT *versus* KO, $p = 0.003$, calculated using one-way ANOVA (*H* and *M*).

**Table 3**

**Passive and active properties of Purkinje cells recorded in acute brain slices of wildtype and GBA2-KO mice**

A current step protocol was used to determine active and passive properties of Purkinje cells recorded in the whole-cell current-clamp configuration. Mean age of wildtype mice, 15.9 ± 0.8 days; mean age of GBA2-KO mice, 15.7 ± 0.5 days. WT, $n = 8$; GBA2-KO, $n = 10$. The Student's $t$ test was used to test statistical significance between WT and KO cells.

| | WT, mean ± S.D. | KO, mean ± S.D. | $p$, WT *vs.* KO |
|---|---|---|---|
| $V_{rest}$ | −54 ± 10 | −49 ± 11 | 0.45 |
| $\tau_m$ (ms) | 116 ± 70 | 98 ± 30 | 0.61 |
| $R_{in,\ peak}$ (megohm) | 170 ± 119 | 110 ± 24 | 0.28 |
| $R_{in,\ steady}$ (megohm) | 79 ± 62 | 43 ± 30 | 0.24 |
| $V_{thresh}$ (mV) | −45 ± 4 | −47 ± 4 | 0.22 |
| A (mV) | 68 ± 9 | 68 ± 7 | 0.91 |
| AHP (mV) | −11 ± 2 | −11 ± 5 | 0.66 |
| FWHM (ms) | 0.63 ± 0.2 | 0.57 ± 0.08 | 0.47 |
| $AP_{freq}$ (Hz) | 60 ± 32 | 54 ± 28 | 0.70 |

uct was amplified in a recombinant PCR, subcloned into pcDNA3.1(+), and verified by sequencing. Primers used for cloning are outlined in Table S1.

### Cell lines and culture

Chinese hamster ovary (CHO) K1 cells were cultured in F-12 medium (ThermoFisher Scientific), containing 10% FCS (Biochrome) and kept at 37 °C, 5% $CO_2$.

Dermal fibroblasts were isolated from mouse tails using collagenase digestion. Tail pieces were incubated in DMEM/GlutaMax (Gibco; 61965-026) containing 10% FCS (Biochrom; S0115), 1 mM sodium pyruvate (Gibco Life Technologies, Inc.; 11360-039), 2 mM L-glutamine (Gibco Life Technologies, Inc.; 25030-024), 100 units/ml penicillin, 100 μg/ml streptomycin (PenStrep; Gibco; 15140-122), 1 mg/ml collagenase (Sigma; C9891) for 3 h at 37 °C and 5% $CO_2$. After digestion, the supernatant was centrifuged for 5 min, 600 × *g* at room temperature. The cell pellet was resuspended in medium, and cells were plated on cell culture plates and cultured at 37 °C, 5% $CO_2$. After 24 h, the medium was changed.

Primary cerebellar neurons were isolated from mouse brains. The cerebella of day P6–11 mice were dissected and directly placed in sterile HBSS (Gibco, catalog no. 14025-053) + 7 mM HEPES (Gibco, catalog no. 15630-56). Meninges were carefully removed using fine forceps, and the cerebellum was minced into small pieces. Tissue was dissociated in 1 ml of trypsin/DNase solution (1% w/v trypsin (Cell Systems, catalog no. LS003703), 1 mg/ml DNase (Roche Applied Science, catalog no. 11284932001), 0.9 mM $MgSO_4$, 1 N NaOH, in CMF-PBS (137 mM NaCl, 4 mM KCl, 11 mM glucose, 4.2 μM $Na_2HPO_4$, 1.8 mM $KH_2PO_4$, 0.004% (w/v) $NaHCO_3$, pH 7.4)) and incubated at room temperature for 10 min. Trypsin was inactivated by addition of 5 ml of DMEM (Gibco catalog no. 31966-021), 5% heat-inactivated horse serum (Pan Biotech, catalog no. P30-0712). Afterward, the tissue was washed three times in HBSS, 7 mM HEPES, in the presence of DNase (0.005 mg/ml). Then, cells were dissociated with glass Pasteur pipettes coated with 4% BSA (Sigma, catalog no. A7906), centrifuged at 800 × *g* for 5 min at 4 °C, and washed twice with HBSS, 7 mM HEPES. Finally, the cells were resuspended in 5 ml of complete neurobasal medium (neurobasal medium (Gibco, catalog no. 12349-015)), 2% (v/v) B-27 supplement (Gibco, catalog no. 17504-044), 2 mM L-glutamine (Gibco; catalog no. 25030-024), 1% PenStrep antibiotic (Gibco, catalog no. 15140122), and 2% horse serum counted and plated on poly-L-lysine–coated coverslips (30,000 cells/1,32 $cm^2$ (= approximately area of the 13-mm coverslip in the 4-well dish)). The cells were kept at 37 °C, 5% $CO_2$.

### Transfection

CHO cells were transfected using polyethyleneimine (Sigma) with 13.16 μg of plasmid DNA per 9-cm dish or 0.7 μg of plasmid DNA per 13-mm coverslip (4-well plate; Lipofectamine 2000 (Invitrogen): mGBA2-R225*-HA, mGBA2-W164*-HA, and mGBA2-Y112*-HA). Mouse fibroblasts ($1 \times 10^6$) were resuspended in 100 μl of transfection buffer (Neon transfection system, Life Technologies, Inc.), and 4 μg of plasmid DNA was added. A microporator mini (Digital Bio Technology, MP-100) was used to electroporate the cells. Here, 10 μl of the cell suspension were subjected to two pulses (20 ms each) of 1000 V and afterward transferred to poly-L-lysine–coated glass-bottom dishes (Mat Tek, catalog no. P35G-1.5-20-C) or on CYTOO chips (CYTOO Cell Architects, catalog no. 10-900-13-06).

### Mice

All animal experiments were conducted according to the German law of animal protection and in agreement with the approval of the local institutional animal care committees (Landesamt für Natur, Umwelt und Verbraucherschutz (LANUV), North Rhine-Westphalia, Az 84-02.04.2014.A194). Mice were maintained under specific pathogen-free conditions and were handled according to protocols approved by the LANUV. The generation of global GBA2-deficient mice has been described elsewhere (3). In addition, a global GBA2-deficient mouse line with conditional potential containing a *lacZ* cassette in the region spanning exons 1–4 of the *Gba2* gene (*Gba2*$^{tm1a(EUCOMM)Wtsi}$, European Conditional Mouse Mutagenesis Program EUCOMM) was used for this study. +/*lacZ* mice were used for matings; the offspring was genotyped by PCR using GBA2- and *lacZ*-specific primers (GBA2: 359 bp with #1 AATGCTAAAGTGGGGATGAAGC and #2 CTGCTCCAGTTCAAGGTCCC; *lacZ*: 108 bp with #1 ATCACGACGCGCTGTATC and #2 ACATCGGGCAAATAATATCG). GBA2-KO mice from both lines did not show any GBA2 expression or activity and displayed the male fertility defect described elsewhere (3, 4).

### Antibodies

The following antibodies were used in this study.

*Primary antibodies*—The following were used: HA (Kremmer R001 3F10: ICC, 1:1000; WB, 1:10,000); HA-7 (Sigma H9658: ICC, 1:500); caveolin-1 (Cell Signaling, 3238, WB, 1:1000); calnexin (Sigma C4731: WB, 1:5000/1:20,000); GAPDH-71.1 (Sigma G9295: WB, 1:30,000); Rac1 (Abcam ab33186: WB, 1:1000); Cdc-42 (Abcam ab64533: WB, 1:1000); FLAG M2 (Sigma F1804: WB, 1:1000/1:2000); β-actin (Abcam 6276: WB, 1:10,000); α-tubulin B-5-2-1 (Sigma T5168: WB, 1:5000); β-tubulin 2.1 (Sigma T4026: WB, 1:1000/1:10,000); tubulin β-III (Biolegend catalog no. 801201: ICC, 1:100).

*Secondary antibodies*—The following were used: WB: IRDye680, IRDye800 (LI-COR: 1:10,000/1:20,000); HRP-conjugated donkey anti-Rb (Dianova 711-035-152: 1:5000); HRP-conjugated goat anti-rat (Dianova 112-035-069: 1:5000); ICC: goat anti-rat IgG H&L Cy3 (Abcam ab6953: 1:400); and goat anti-mouse Alexa Fluor 488 (Molecular Probes, catalog no. A11029).

The following dyes were used: Alexa Fluor 488 phalloidin (Life Technologies, Inc., catalog no. A12379; ICC: 1:250); rhodamine-conjugated phalloidin (Life Technologies, Inc., catalog no. R415; ICC: 1:500); and DAPI (Life Technologies, Inc., D1306; ICC: 1:10,000).

### Protein preparation

All steps were performed at 4 °C in the presence of a mammalian protease inhibitor mixture (mPIC, Sigma). Tissues were homogenized in hypotonic buffer (10 mM HEPES, 0.5 mM EDTA, pH 7.4, 0.1 g/ml wet weight) using an Ultra-turrax (IKA) or tissue douncer and three pulses (20 s each) of sonification in ice-cold water (Branson sonifier). Tissue suspensions were subjected to low-speed centrifugation for 20 min at 1000 × *g*. The supernatant (post-nuclear supernatant) was used for activity assays (2-cm cell culture dish and cells were pelleted for 5 min at 500 × *g* and 4 °C. Afterward, the pellets were directly lysed in hypotonic buffer, sonicated, and used for activity assays or Western blot analysis. Protein concentration was determined using the Bradford assay or the bicinchoninic acid (BCA) test kit (Pierce) according to the manufacturer's protocol.

### Western blot analysis

Western blot analysis was performed as described elsewhere (2). Protein expression was quantified using ImageJ (version 1.48, Wayne Rasband, National Institutes of Health). As the protein standard, protein marker VI (10–245 kDa, AppliChem), HiMark protein standard (ThermoFisher Scientific), or Biomol marker (catalog no. 10009) was used.

To analyze Rho GTPase activity, samples were suspended in SDS sample buffer and separated using 4–12% NuPAGE Novex BisTris gradient gels (Life Technologies, Inc.) with a thickness of 1.5 mm. Electrophoresis was performed in MOPS running buffer (Invitrogen, NP0001) in an XCell SureLock mini gel chamber (Life Technologies, Inc.) at 120 mA and 180 V.

### Co-immunoprecipitation

All steps were performed at 4 °C in the presence of mPIC (Sigma). Transfected cells from a 9-cm plate were lysed in 200 μl of detergent-containing lysis buffer (10 mM Tris/HCl, pH 7.5, 150 mM NaCl, 0.5 mM EDTA, 1% Triton X-100). Lysate was centrifuged at 10,000 × *g* for 5 min, and supernatant was taken for further steps. BCA test was performed, and 20 μl of the lysate was taken as input/input 1 for Western blot analysis. Pre-clearing on underivatized agarose matrix was performed using cyanogen bromide–activated agarose (Sigma), which has been prepared as a 50% (w/v) suspension with 50% (v/v) glycerol in 10 mM sodium phosphate buffer, pH 7.4, 150 mM NaCl, 0.02% (w/v) sodium azide. 50 μl of matrix suspension was centrifuged at 14,000 × *g* to remove the buffer and equilibrated in 5× column volume (CV) equilibration buffer and 5× CV lysis buffer. 250 μg of protein in a total volume of 500 μl was added to the matrix and incubated for 5–6 h end-over-end. Agarose matrix was then pelleted at 14,000 × *g*, and 20 μl were taken as input (input 2) for Western blot analysis. The remaining supernatant was loaded on anti-FLAG magnetic beads (Sigma; 50 μl of bead slurry equilibrated in 5× CV equilibration buffer, 5× CV lysis buffer). Lysate was incubated on the beads overnight end-over-end at 4 °C. Afterward, suspension was magnetically separated, and supernatant was taken as NonBound for Western blot analysis. Magnetic particles were washed four times with 300 μl of washing buffer (10 mM Tris/HCl, pH 7.5, 500 mM NaCl, 0.5 mM EDTA, 1% Triton X-100). An aliquot of the supernatant of the initial/final washing step was taken for Western blot analysis. Finally, bead-bound protein was eluted in 2× CV of 0.1 M glycine, pH 3.0, during incubation at room temperature end-over-end. Immediately after magnetic separation, supernatant was transferred to 16.67 μl of 1 M Tris/HCl, pH 8.0, for neutralization and subjected to Western blotting as the eluate.

### Cross-linking experiments

All steps were performed at 4 °C in the presence of mPIC (Sigma). Transfected cells were lysed in 10 mM HEPES/NaOH, pH 7.4, and sonicated in ice-cold water in three pulses (20 s each) (Branson sonicator). Protein concentration was determined in a BCA test. As a chemical cross-linker, 20 mM disuccinimidyl suberate (DSS; ThermoFisher Scientific) was prepared in DMSO. 40 μg of protein in 40-μl total volume was incubated with 0.77 mM DSS for 2 h at 4 °C. Reaction was stopped by adding 12 μl of 1 M Tris/HCl, pH 7.5 (final concentration of 0.22 M). SDS-sample buffer was added, and 40 μg of protein (= complete sample volume) was subjected to Western blot analysis (without boiling before loading).

### Structural modeling

Structural models of human GBA2 and missense mutations in GBA2 were achieved using the workspace mode of the SWISS-MODEL suite (21). Homology modeling was performed on the crystal structure of *Tx*GH116 β-glucosidase (PDB accession code 5BVU). A continuous model was built from residues 77 to 888. The ligand β-D-glucose was superimposed into the models of hGBA2 from the crystal structure 5BX5 (19).

### β-Glucosidase activity assay

The assay was performed as described elsewhere (2, 24). For AMP-DNM (27), 30 pM was used in the assay in a 25-μl sample volume, which, after addition of 5 μl of 4-MUG, resulted in a final concentration of 25 pM.

### Treatments

Neurons were treated with 5 μM NB-DNJ (Sigma) or 30 pM AMP-DNM (27). Fibroblasts were treated with 2 μM NB-DNJ for 48 h to inhibit GBA2, 100 μM NCS23766 (Tocris, 2161) for 2 h to inhibit Rac1, and 10 μM ML141 (Calbiochem, 217708) for 1 h to inhibit Cdc-42.

### Immunohistochemistry and ICC

Mouse fibroblasts were plated on CYTOO chips (CYTOO Cell Architects, catalog no. 10-900-13-06) placed in a 35-mm cell culture plate. Cells were fixed with 4% paraformaldehyde and labeled with Alexa Fluor 488 phalloidin and DAPI. Images were taken using an Olympus FV1000 confocal microscope.

Neurons were fixed in 4% PFA for 15 min at room temperature. Residual PFA was quenched for 10 min with 50 mM $NH_4Cl$. Afterward, cells were permeabilized for 3 min with 0.1% Triton X-100, followed by 30 min blocking in 2% FCS, 2% BSA, 0.2% fish gelatin. Primary and secondary antibodies were incubated for 1 h or 30 min, respectively, in 10% blocking solution. Finally, cells were mounted using Fluoromount (Sigma, catalog no. F4680). Between all steps, cells were washed three times with PBS.

Mice were anesthetized by intraperitoneal injection of 100 mg/kg body weight ketamine (Medistar) and 10 mg/kg body weight xylazine (Ceva). Thoracotomy was performed, and mice were perfused with 4% PFA (approved by LANUV Az 84-02.04.2017.A246). Brain and spinal cord were dissected and fixed overnight in 4% PFA at 4 °C. Tissue used for X-gal staining was dissected from nonperfused mice and fixed for 7 days in 0.2% glutaraldehyde in PBS. After washing in PBS (10 min at room temperature), tissue was cryo-preserved in a sucrose gradient (10% sucrose in PBS for 1 h at room temperature; 30% sucrose in PBS overnight at 4 °C). Brain tissue was frozen without embedding, and spinal cord was embedded in Tissue Tek (Sakura), frozen on dry ice, and stored at −80 °C for long term. 16-$\mu$m sagittal and coronal brain sections (caudal region) and 16-$\mu$m transverse sections of the cervical spinal cord were sliced using the cryostat (Mikrom HM560, ThermoFisher Scientific) and frozen at −20 °C until further use.

### X-gal staining

Cells were fixed for 5 min in 0.2% glutaraldehyde. Fixed cells/tissue sections were washed three times for 5 min with LacZ wash solution (0.1% (w/v) sodium deoxycholate, 0.2% (v/v) Igepal CA-630 in LacZ basis solution: 77 mM $Na_2HPO_4$, 23 mM $NaH_2PO_4$, 1.25 mM $MgCl_2$, 2 mM EGTA). Cells/tissue sections were then incubated with 0.01% (w/v) or 0.05% (w/v) X-gal (dissolved in DMF) in pre-warmed LacZ staining solution (5 mM $K_3[Fe(CN)_6]$, 5 mM $K_4[Fe(CN)_6]$ in LacZ basis solution) overnight in a humidified chamber at 37 °C in an incubator without controlled $CO_2$ supply. Cells/tissue sections were washed twice with $H_2O$ and mounted on glass slides using Aqua-Poly/Mount (Polysciences, Inc.). Stained cells/sections were imaged using the Nikon Eclipse Ti microscope (stitching mode for tissue sections).

### Nissl staining

Slide-mounted tissue was demyelinated in a graded alcohol series (70% EtOH, 95% EtOH, 100% EtOH; 5 min each) and subsequently rehydrated (95% EtOH, 70% EtOH, 50% EtOH; 5 min each). Short rinsing in $H_2O$ was followed by cresyl violet acetate staining (filtered 1% cresyl violet acetate (Sigma), 1% acetic acid) for 4 min. Slides were washed in $H_2O$ three times (30 s each) to remove excess stain and shortly washed in 70% EtOH and 95% EtOH. For differentiation of the staining, tissue sections were shortly incubated in 95% EtOH, 1% acetic acid, then dehydrated in 95% EtOH and 100% EtOH. Finally, sections were cleared in xylol (Isomere, Roth) and mounted with Entellan® (Merck). Stained sections were imaged using the Nikon Eclipse Ti microscope (stitching mode).

### Analysis of cytoskeletal structures

For fibroblasts, filopodia (slender actin-protrusions) and lamellipodia (wave-like actin extensions) structures were counted. For neurons, neurite length of the neuronal tubulin $\beta$-III–positive protrusions was measured.

### Rho GTPase activity assay

Fibroblasts (3× confluent 9-cm plates) were lysed in 750 $\mu$l of lysis buffer (50 mM Tris, pH 7.5, 10 mM $MgCl_2$, 0.5 M NaCl, 2% Igepal) in the presence of a mammalian protease inhibitor mixture mPIC (Sigma) within 5 min to prevent Rho GTPase degradation and frozen until the assay was performed. For the assay, 400 $\mu$g of the lysate was used to measure Rac1-GTP, and 300 $\mu$g of the lysate was used to measure Cdc42-GTP. Volume of lysate was adjusted to 0.5 $\mu$g/$\mu$l with cold lysis buffer. 10 $\mu$g of GST-tagged PAK-PBD protein (Cytoskeleton, PAK01-A) was added to the lysate and incubated for 30 min at 4 °C on a rotator. 25 $\mu$l of GSH-Sepharose beads (GE Healthcare catalog no. 17-0756-05) were incubated with the lysate for 30 min at 4 °C on a rotator. Samples were centrifuged at 8000 × *g* for 1 min at 4 °C. The pellet was washed in wash buffer (25 mM Tris, pH 7.5, 30 mM $MgCl_2$, 40 mM NaCl, mPIC), resuspended in 25 $\mu$l of 2× SDS-PAGE loading buffer, and analyzed by Western blotting. 10 $\mu$g of the original lysate was used as input. Lysates loaded with GTP or GDP (Cytoskeleton, BK035) were used as positive and negative controls, respectively. Here, prior to PAK-GST incubation, lysates were treated with 15 mM EDTA to facilitate nucleotide exchange, followed by addition of 200 $\mu$M GTP or GDP and then 60 mM $MgCl_2$ to quench the exchange.

### Isolation of DRM fractions

Separation of detergent-resistant membrane fractions was adapted from an earlier publication (52). 3 × $10^6$ fibroblasts were pelleted and frozen until analyzed. 5× TNE buffer was prepared freshly before each experiment (750 mM NaCl, 10 mM EDTA, 250 mM Tris-HCl, pH 7.4). Each cell pellet was resuspended in 700 $\mu$l of TNE buffer (1×), containing mPIC, and lysed mechanically using a syringe with a 24-gauge needle (25 strokes) on ice. 315 $\mu$l of the lysate was transferred to a new tube; 35 $\mu$l of 10× Triton X-100 (prepared in 1× TNE buffer; final concentration 1×) were added, mixed gently, and left on ice for 30 min. To this lysate, 700 $\mu$l of 60% iodoxanol (40% final concentration; OptiPrep, Sigma, D1556) was added, mixed, and transferred into an ultracentrifuge tube (Beckman, 349623). Here, a gradient was established by overlaying the lysate containing 40% iodoxanol first with 2.1 ml of 30% iodoxanol (prepared by diluting 60% iodoxanol in 2× TNE buffer in a ratio of 1:1) and second with 350 $\mu$l of 1× TNE buffer. All solutions contained mPIC. The sample was centrifuged at 260,000 × *g* for 2 h at 4 °C in an SW-55 Ti rotor (Beckman Coulter, 342196).

After ultracentrifugation, the samples were separated into three equal fractions of 1167 μl each (top, middle, and bottom) and analyzed by Western blotting.

### Quantification of lipids using MS

Quantification of lipids using MS was performed as described before (24). Alternatively, sphingolipid analysis was carried out using a QTRAP 6500+ LC-MS/MS system (Sciex, Darmstadt) with a Turbo V ion source. Sphingolipids were delivered to the MS via an M3 MicroLC (Sciex, Darmstadt) at a flow rate of 10 μl/min. The gradient method was modified from Ref. 53. The sample was infused into the source using a constant flow of 100% solvent A (methanol) from 0 to 10 min. All remaining components were washed out with 100% solvent B (methanol/acetic acid, 9:1, v/v) from 10.1 to 12 min. Re-equilibration was achieved with 100% solvent A from 12.1 to 15 min. Samples were dissolved in 100 μl of isopropyl alcohol, chloroform, methanol, 300 mM ammonium acetate in water, 25:30:41.5:3.5, v/v/v/v) (53). Sphingolipids were detected in the positive ion mode with the following instrument settings: curtain gas, 20 p.s.i.; collision gas, medium; IonSpray voltage, 5500 V; ion source temperature, 150 °C; nebulizer and turbogas, 25 p.s.i. The parameters for MRM transitions were as follows: declustering potential, 70 V; entrance potential, 10 V; cell exit potential, 12 V; collision energies, 15 V (long-chain bases), 35 V (Cer), and 40 V (HexCer). Data evaluation was carried out using the MultiQuant 3.0.2 software. For quantification of sphingolipids, the peak areas of the chromatograms resulting from MRMs were compared with those of the internal standards.

### Extraction of lipids and TLC

Tissue lysates corresponding to 2–3 mg of protein content were transferred into 2-ml Eppendorf tubes, lyophilized, and suspended in 1 ml of methanol using a metal bead and a Tissue Lyser. After addition of 1 ml of chloroform, samples were incubated at 37 °C for 15 min in an ultrasonic bath and centrifuged at 12,000 × *g* for 5 min. The supernatant was collected, and the pellet was re-extracted with 2 ml of chloroform/methanol/water (10:10:1) and with 2 ml of chloroform/methanol/water (30:60:8). The second and third supernatants were pooled with the first supernatant. From this raw extract, acidic lipids were separated from neutral lipids using DEAE-25 columns with a 100-μl bed volume and desalted on reversed phase C18 columns as described before (25). Gangliosides of the acidic fraction were further enriched by mild alkaline treatment, *i.e.* 0.1 M KOH in methanol for 2 h at 37 °C, neutralized with acetic acid, and desalted on reversed phase columns. The ganglioside fraction was dried under a gentle nitrogen stream at 37 °C and dissolved in chloroform/methanol/water (10:10:1) at a concentration of 1 mg of protein/100 μl.

### Electrophysiology

*Acute brain slices*—For electrophysiological brain-slice recordings, P15–17 WT or GBA2-KO mice were anesthetized with isofluorane (Baxter) and decapitated. The cerebellum was carefully removed and placed in ice-cold artificial cerebrospinal fluid (ACSF), containing in mM: NaCl 125, $NaHCO_3$ 25, D-glucose 25, KCl 2.5, $NaH_2PO_4$ 1.25, $CaCl_2$ 2, and $MgCl_2$ 1. 250-μm thick sagittal slices were cut on a Leica VT1200S vibratome (Leica). The slices were then incubated at 37 °C for 45 min and kept at room temperature until transfer to the recording chamber. The slices were kept in ACSF continuously bubbled with 5% $CO_2$ and 95% $O_2$ to maintain pH 7.4. Brain slices were visualized under an upright BX51WI light microscope (Olympus), equipped with a ×40 water immersion objective (LUMPlan FI/IR, Olympus). Whole-cell current-clamp recordings were performed with a Multiclamp 700B amplifier (Molecular Devices) connected via a Digidata 1440A acquisition board (Molecular Devices) to a PC running pClamp (Molecular Devices). Data were low-pass–filtered at 5 kHz and sampled at 10 kHz. All recordings were conducted at room temperature. Patch pipettes were pulled from borosilicate capillaries (Hilgenberg) using a DMZ puller (Zeitz Instruments GmbH) and filled with intracellular solution, containing in mM: potassium gluconate 110, KCl 10, $Na_2$-phosphocreatine 7, Mg-ATP 4, Na-GTP 0.3, HEPES 10, D-mannitol 45, Alexa Fluor 488 0.1, titrated with KOH to pH 7.32 (300 mOsm). Patch pipettes had an initial resistance of 5–10 megohms.

Recordings were analyzed with Igor Pro (Wavemetrics). Resting membrane potential ($V_{rest}$) was measured immediately after breaking into the cell. If necessary, a negative holding current was injected to keep the cells at −70 mV during recordings. From the holding current, current steps of increasing amplitude (25 pA, starting from −200 pA) were applied. The first three steps (−200, −175, and −150 pA) were used to calculate the input resistance ($R_{in}$) at the peak and at the steady state of the membrane potential. Rheobase indicates the smallest current step sufficient to trigger action potentials (APs). The membrane time constant $\tau$ ($\tau_m$) was calculated from a monoexponential fit of the membrane potential following the recovery from a 2-ms current step to −2000 pA (Fig. 5*G*). AP properties were calculated from APs triggered by current injections around the rheobase. The action potential threshold $V_{thresh}$ was defined as the voltage where the temporal derivative of the voltage exceeds 30 mV/ms. The AP amplitude was calculated as the difference between $V_{thres}$ and the peak voltage. The after-hyperpolarization potential (AHP) was calculated as the difference between $V_{thresh}$ and the minimal membrane potential following the AP (Fig. 5*F*). The full-width at half-maximum (FWHM) was measured as the width of the AP at the half-amplitude voltage. The maximal AP firing rate was determined for the maximal current injection at which the neurons fired continuously.

*Primary cerebellar cultures*—Whole-cell current-clamp recordings of primary cerebellar neurons were conducted 48 h after dissection. We chose cells that were fairly isolated and not part of cell clusters. Those cells did not fire APs. During recordings, cells were kept in a continuously perfused recording chamber, mounted on an inverted IX71 microscope (Olympus). Recording solutions and patch pipettes were the same as the ones for acute brain slice recordings. Data were acquired using an Axopatch 200B amplifier (Molecular Devices) connected via a Digidata 1440A acquisition board to a PC running pClamp. Recordings were low-pass–filtered at 5 kHz and sam-

pled at 10 kHz. $V_{rest}$ was measured immediately after whole-cell configuration was established. Currents from −3 to −10 pA were injected to determine $\tau_m$ and $R_{in}$.

### Behavioral experiments

*Weight test*—The weight test was performed in the animal facility of Caesar on 3 consecutive days. Mice had to grasp a steel chain of 1) 21 g, 2) 34.8 g, 3) 48.6 g, 4) 62.4 g, 5) 75.5 g, 6) 89 g, and 7) 103.3 g with their forepaws while being held by the tail and lifted. If the mouse held the weight for 3 s, the next heavier weight was used. If a mouse failed to hold it for 3 s and dropped the weight, it was tested on the same weight after resting for at least 10 s. The trial was terminated when the mouse failed three times, and the time the mouse was able to hold this maximum weight was noted. Based on these data, the relative muscle strength unit (rsu) was calculated as follows: $x$ (rsu) = $n \times 3$ (seconds) + $t$ (seconds), where $x$ is the muscle strength (in rsu); $n$ is the weight the mouse could hold for 3 s; and $t$ is the time (seconds) it held the next heavier failed weight.

*CatWalk*—The CatWalk system (CatWalk™ XT 9.0 and 10.6, Noldus Information Technologies) was used to determine gait parameters of mice. Before the experiment, the camera-walkway distance was set to 40 cm and the corridor width to 5.5 cm, and the system was calibrated using a calibration sheet of known dimensions (20 × 10 cm). The camera gain was set to 20.00 db (CatWalk XT 10.6) or 30.00 db (CatWalk XT 9.0), and the green intensity threshold was set to 0.1 to define the maximum and minimum green intensity to detect the paws; additionally, in the CatWalk XT 10.6 software, the red ceiling light was set to 17.7 V and the green walking light to 16.0 V (CatWalk™ 10.6). The experiment was performed in the dark on 3 consecutive days in the morning after the animals habituated to the walkway 1 day before, and two compliant runs (maximum speed variation: 60%) per day with four consecutive steps of each paw were classified for gait analysis. The following gait parameters were plotted based on the classified paws: swing duration and phase dispersion were according to Ref. 46, and step pattern. Swing duration of the GBA2-KO (KO) mice was plotted relative to the corresponding wildtype (WT) tested with the same software (CatWalk 9.0 or 10.6) or for the interpaw coordination parameter phase dispersion and step pattern as averaged values for WT and KO or individual values for each animal over all experiments, respectively. After completion of all behavior experiments, mice were euthanized by anesthetizing with isofluorane (Baxter) followed by cervical dislocation. Dissected tissues were frozen at −80 °C for long-term storage. Genotypes of all tested mice were validated in a β-glucosidase activity assay performed with hypotonic brain lysates.

### Statistical analysis

Results are presented as mean ± S.D. Statistical analysis was performed using Origin Pro 9.0 (one-way ANOVA or one-sample Student's $t$ test). $p$ values are only indicated when considered significant (≤0.05).

*Author contributions*—M. A. W., P. D., J. N. H., J. M. A., H. E., R. S., M. G., T. K. B., F. B., and D. W. conceptualization; M. A. W., S. Stern, D. N. R., E. G., D. D., K. G., S. Schonauer, C. E. M., R. S., T. K. B., and D. W. formal analysis; M. A. W., S. Stern, D. N. R., E. G., D. D., K. G., S. Schonauer, C. E. M., H. G. K., R. S., M. G., and D. W. validation; M. A. W., C. E. M., M. G., T. K. B., and D. W. investigation; M. A. W., D. N. R., E. G., D. D., K. G., H. H., M. G., and D. W. visualization; M. A. W., D. N. R., E. G., D. D., P. D., J. N. H., S. Schonauer, C. E. M., H. G. K., J. M. A., W. B., H. E., R. S., M. G., T. K. B., F. B., and D. W. methodology; M. A. W., S. Stern, D. N. R., J. N. H., S. Schonauer, C. E. M., H. H., H. G. K., J. M. A., W. B., H. E., R. S., M. G., T. K. B., F. B., and D. W. writing-review and editing; S. Stern, D. N. R., E. G., K. G., C. E. M., T. K. B., F. B., and D. W. data curation; P. D., J. N. H., S. Schonauer, H. H., H. G. K., J. M. A., W. B., H. E., R. S., M. G., T. K. B., F. B., and D. W. resources; J. N. H., H. H., H. E., and M. G. software; S. Schonauer, H. G. K., W. B., H. E., T. K. B., F. B., and D. W. supervision; D. W. funding acquisition; D. W. writing-original draft; D. W. project administration.

*Acknowledgments—We thank J. H. Krause, I. Lux, D. Herborn, M. Völker, and J. Görgen for technical assistance; J. F. Jikeli for help with data analysis; the DZNE animal facility for help with the behavioral assay; and the LIMES GRC for generating the GBA2-Eucomm mice. We thank Paulo Gaspar, Andre Margues, and Maria Joao Ferraz from the Aerts laboratory for the GlcChol measurements.*

## References

1. Boot, R. G., Verhoek, M., Donker-Koopman, W., Strijland, A., van Marle, J., Overkleeft, H. S., Wennekes, T., and Aerts, J. M. (2007) Identification of the non-lysosomal glucosylceramidase as β-glucosidase 2. *J. Biol. Chem.* **282,** 1305–1312 CrossRef Medline
2. Körschen, H. G., Yildiz, Y., Raju, D. N., Schonauer, S., Bönigk, W., Jansen, V., Kremmer, E., Kaupp, U. B., and Wachten, D. (2013) The non-lysosomal β-glucosidase GBA2 is a non-integral membrane-associated protein at the endoplasmic reticulum (ER) and Golgi. *J. Biol. Chem.* **288,** 3381–3393 CrossRef Medline
3. Yildiz, Y., Matern, H., Thompson, B., Allegood, J. C., Warren, R. L., Ramirez, D. M., Hammer, R. E., Hamra, F. K., Matern, S., and Russell, D. W. (2006) Mutation of β-glucosidase 2 causes glycolipid storage disease and impaired male fertility. *J. Clin. Invest.* **116,** 2985–2994 CrossRef Medline
4. Raju, D., Schonauer, S., Hamzeh, H., Flynn, K. C., Bradke, F., Vom Dorp, K., Dörmann, P., Yildiz, Y., Trötschel, C., Poetsch, A., Breiden, B., Sandhoff, K., Körschen, H. G., and Wachten, D. (2015) Accumulation of glucosylceramide in the absence of the β-glucosidase GBA2 alters cytoskeletal dynamics. *PLoS Genet.* **11,** e1005063 CrossRef Medline
5. van der Spoel, A. C., Jeyakumar, M., Butters, T. D., Charlton, H. M., Moore, H. D., Dwek, R. A., and Platt, F. M. (2002) Reversible infertility in male mice after oral administration of alkylated imino sugars: a nonhormonal approach to male contraception. *Proc. Natl. Acad. Sci. U.S.A.* **99,** 17173–17178 CrossRef Medline
6. Walden, C. M., Butters, T. D., Dwek, R. A., Platt, F. M., and van der Spoel, A. C. (2006) Long-term non-hormonal male contraception in mice using *N*-butyldeoxynojirimycin. *Hum. Reprod.* **21,** 1309–1315 CrossRef Medline
7. Walden, C. M., Sandhoff, R., Chuang, C. C., Yildiz, Y., Butters, T. D., Dwek, R. A., Platt, F. M., and van der Spoel, A. C. (2007) Accumulation of glucosylceramide in murine testis, caused by inhibition of β-glucosidase 2: implications for spermatogenesis. *J. Biol. Chem.* **282,** 32655–32664 CrossRef Medline
8. Aureli, M., Gritti, A., Bassi, R., Loberto, N., Ricca, A., Chigorno, V., Prinetti, A., and Sonnino, S. (2012) Plasma membrane-associated glycohydrolases along differentiation of murine neural stem cells. *Neurochem. Res.* **37,** 1344–1354 CrossRef Medline

9. Herrera Moro Chao, D., Kallemeijn, W. W., Marques, A. R., Orre, M., Ottenhoff, R., van Roomen, C., Foppen, E., Renner, M. C., Moeton, M., van Eijk, M., Boot, R. G., Kamphuis, W., Hol, E. M., Aten, J., Overkleeft, H. S., *et al.* (2015) Visualization of active glucocerebrosidase in rodent brain with high spatial resolution following *in situ* labeling with fluorescent activity based probes. *PLoS ONE* **10,** e0138107 CrossRef Medline
10. Citterio, A., Arnoldi, A., Panzeri, E., D'Angelo, M. G., Filosto, M., Dilena, R., Arrigoni, F., Castelli, M., Maghini, C., Germiniasi, C., Menni, F., Martinuzzi, A., Bresolin, N., and Bassi, M. T. (2014) Mutations in CYP2U1, DDHD2 and GBA2 genes are rare causes of complicated forms of hereditary spastic paraparesis. *J. Neurol.* **261,** 373–381 CrossRef Medline
11. Hammer, M. B., Eleuch-Fayache, G., Schottlaender, L. V., Nehdi, H., Gibbs, J. R., Arepalli, S. K., Chong, S. B., Hernandez, D. G., Sailer, A., Liu, G., Mistry, P. K., Cai, H., Shrader, G., Sassi, C., Bouhlal, Y., *et al.* (2013) Mutations in GBA2 cause autosomal-recessive cerebellar ataxia with spasticity. *Am. J. Hum. Genet.* **92,** 245–251 CrossRef Medline
12. Haugarvoll, K., Johansson, S., Rodriguez, C. E., Boman, H., Haukanes, B. I., Bruland, O., Roque, F., Jonassen, I., Blomqvist, M., Telstad, W., Månsson, J. E., Knappskog, P. M., and Bindoff, L. A. (2017) GBA2 mutations cause a Marinesco-Sjogren-Like syndrome: genetic and biochemical studies. *PLoS ONE* **12,** e0169309 CrossRef Medline
13. Martin, E., Schüle, R., Smets, K., Rastetter, A., Boukhris, A., Loureiro, J. L., Gonzalez, M. A., Mundwiller, E., Deconinck, T., Wessner, M., Jornea, L., Oteyza, A. C., Durr, A., Martin, J. J., Schöls, L., *et al.* (2013) Loss of function of glucocerebrosidase GBA2 is responsible for motor neuron defects in hereditary spastic paraplegia. *Am. J. Hum. Genet.* **92,** 238–244 CrossRef Medline
14. Votsi, C., Zamba-Papanicolaou, E., Middleton, L. T., Pantzaris, M., and Christodoulou, K. (2014) A novel GBA2 gene missense mutation in spastic ataxia. *Ann. Hum. Genet.* **78,** 13–22 CrossRef Medline
15. Harding, A. E. (1983) Classification of the hereditary ataxias and paraplegias. *Lancet* **1,** 1151–1155 Medline
16. Schüle, R., and Schöls, L. (2011) Genetics of hereditary spastic paraplegias. *Semin. Neurol.* **31,** 484–493 CrossRef Medline
17. Woeste, M. A., and Wachten, D. (2017) The enigmatic role of GBA2 in controlling locomotor function. *Front. Mol. Neurosci.* **10,** 386 CrossRef Medline
18. Sultana, S., Reichbauer, J., Schüle, R., Mochel, F., Synofzik, M., and van der Spoel, A. C. (2015) Lack of enzyme activity in GBA2 mutants associated with hereditary spastic paraplegia/cerebellar ataxia (SPG46). *Biochem. Biophys. Res. Commun.* **465,** 35–40 CrossRef Medline
19. Charoenwattanasatien, R., Pengthaisong, S., Breen, I., Mutoh, R., Sansenya, S., Hua, Y., Tankrathok, A., Wu, L., Songsiriritthigul, C., Tanaka, H., Williams, S. J., Davies, G. J., Kurisu, G., and Cairns, J. R. (2016) Bacterial β-glucosidase reveals the structural and functional basis of genetic defects in human glucocerebrosidase 2 (GBA2). *ACS Chem. Biol.* **11,** 1891–1900 CrossRef Medline
20. Artola, M., Wu, L., Ferraz, M. J., Kuo, C. L., Raich, L., Breen, I. Z., Offen, W. A., Codée, J. D. C., van der Marel, G. A., Rovira, C., Aerts, J. F. M. G., Davies, G. J., and Overkleeft, H. S. (2017) 1,6-Cyclophellitol cyclosulfates: a new class of irreversible glycosidase inhibitor. *ACS Cent. Sci.* **3,** 784–793 CrossRef Medline
21. Waterhouse, A., Bertoni, M., Bienert, S., Studer, G., Tauriello, G., Gumienny, R., Heer, F. T., de Beer, T. A. P., Rempfer, C., Bordoli, L., Lepore, R., and Schwede, T. (2018) SWISS-MODEL: homology modelling of protein structures and complexes. *Nucleic Acids Res.* **46,** W296–W303 CrossRef Medline
22. Gudmundsson, M., Hansson, H., Karkehabadi, S., Larsson, A., Stals, I., Kim, S., Sunux, S., Fujdala, M., Larenas, E., Kaper, T., and Sandgren, M. (2016) Structural and functional studies of the glycoside hydrolase family 3 β-glucosidase Cel3A from the moderately thermophilic fungus *Rasamsonia emersonii*. *Acta Crystallogr. D Struct. Biol.* **72,** 860–870 CrossRef Medline
23. Esen, A., and Gungor, G. (1991) Detection of β-glucosidase activity on sodium dodecyl sulphate-polyacrylamide gels. *Appl. Theor. Electrophor.* **2,** 63–69 Medline
24. Schonauer, S., Körschen, H. G., Penno, A., Rennhack, A., Breiden, B., Sandhoff, K., Gutbrod, K., Dörmann, P., Raju, D. N., Haberkant, P., Gerl, M. J., Brügger, B., Zigdon, H., Vardi, A., Futerman, A. H., *et al.* (2017) Identification of a feedback loop involving β-glucosidase 2 and its product sphingosine sheds light on the molecular mechanisms in Gaucher disease. *J. Biol. Chem.* **292,** 6177–6189 CrossRef Medline
25. Sandhoff, R., Hepbildikler, S. T., Jennemann, R., Geyer, R., Gieselmann, V., Proia, R. L., Wiegandt, H., and Grone, H. J. (2002) Kidney sulfatides in mouse models of inherited glycosphingolipid disorders: determination by nano-electrospray ionization tandem mass spectrometry. *J. Biol. Chem.* **277,** 20386–20398 CrossRef Medline
26. Yildiz, Y., Hoffmann, P., Vom Dahl, S., Breiden, B., Sandhoff, R., Niederau, C., Horwitz, M., Karlsson, S., Filocamo, M., Elstein, D., Beck, M., Sandhoff, K., Mengel, E., Gonzalez, M. C., Nöthen, M. M., *et al.* (2013) Functional and genetic characterization of the non-lysosomal glucosylceramidase 2 as a modifier for Gaucher disease. *Orphanet J. Rare Dis.* **8,** 151 CrossRef Medline
27. Overkleeft, H. S., Renkema, G. H., Neele, J., Vianello, P., Hung, I. O., Strijland, A., van der Burg, A. M., Koomen, G. J., Pandit, U. K., and Aerts, J. M. (1998) Generation of specific deoxynojirimycin-type inhibitors of the non-lysosomal glucosylceramidase. *J. Biol. Chem.* **273,** 26522–26527 CrossRef Medline
28. Hamers, F. P., Koopmans, G. C., and Joosten, E. A. (2006) CatWalk-assisted gait analysis in the assessment of spinal cord injury. *J. Neurotrauma* **23,** 537–548 CrossRef Medline
29. Coarelli, G., Romano, S., Travaglini, L., Ferraldeschi, M., Nicita, F., Spadaro, M., Fornasiero, A., Frontali, M., Salvetti, M., Bertini, E., and Ristori, G. (2018) Novel homozygous GBA2 mutation in a patient with complicated spastic paraplegia. *Clin. Neurol. Neurosurg.* **168,** 60–63 CrossRef Medline
30. van der Spoel, A. C., Mott, R., and Platt, F. M. (2008) Differential sensitivity of mouse strains to an *N*-alkylated imino sugar: glycosphingolipid metabolism and acrosome formation. *Pharmacogenomics* **9,** 717–731 CrossRef Medline
31. Bone, W., Walden, C. M., Fritsch, M., Voigtmann, U., Leifke, E., Gottwald, U., Boomkamp, S., Platt, F. M., and van der Spoel, A. C. (2007) The sensitivity of murine spermiogenesis to miglustat is a quantitative trait: a pharmacogenetic study. *Reprod. Biol. Endocrinol.* **5,** 1 CrossRef Medline
32. Kuter, D. J., Mehta, A., Hollak, C. E., Giraldo, P., Hughes, D., Belmatoug, N., Brand, M., Muller, A., Schaaf, B., Giorgino, R., and Zimran, A. (2013) Miglustat therapy in type 1 Gaucher disease: clinical and safety outcomes in a multicenter retrospective cohort study. *Blood Cells Mol. Dis.* **51,** 116–124 CrossRef Medline
33. Pastores, G. M., Giraldo, P., Chérin, P., and Mehta, A. (2009) Goal-oriented therapy with miglustat in Gaucher disease. *Curr. Med. Res. Opin.* **25,** 23–37 CrossRef Medline
34. Shemesh, E., Deroma, L., Bembi, B., Deegan, P., Hollak, C., Weinreb, N. J., and Cox, T. M. (2015) Enzyme replacement and substrate reduction therapy for Gaucher disease. *Cochrane Database Syst. Rev.* ***2015,*** CD010324 CrossRef Medline
35. Ferreirinha, F., Quattrini, A., Pirozzi, M., Valsecchi, V., Dina, G., Broccoli, V., Auricchio, A., Piemonte, F., Tozzi, G., Gaeta, L., Casari, G., Ballabio, A., and Rugarli, E. I. (2004) Axonal degeneration in paraplegin-deficient mice is associated with abnormal mitochondria and impairment of axonal transport. *J. Clin. Invest.* **113,** 231–242 CrossRef Medline
36. Soderblom, C., Stadler, J., Jupille, H., Blackstone, C., Shupliakov, O., and Hanna, M. C. (2010) Targeted disruption of the Mast syndrome gene SPG21 in mice impairs hind limb function and alters axon branching in cultured cortical neurons. *Neurogenetics* **11,** 369–378 CrossRef Medline
37. Nowak, A., Mechtler, T. P., Hornemann, T., Gawinecka, J., Theswet, E., Hilz, M. J., and Kasper, D. C. (2018) Genotype, phenotype and disease severity reflected by serum LysoGb3 levels in patients with Fabry disease. *Mol. Genet. Metab.* **123,** 148–153 CrossRef Medline
38. Harel, R., and Futerman, A. H. (1993) Inhibition of sphingolipid synthesis affects axonal outgrowth in cultured hippocampal neurons. *J. Biol. Chem.* **268,** 14476–14481 Medline
39. Furuya, S., Ono, K., and Hirabayashi, Y. (1995) Sphingolipid biosynthesis is necessary for dendrite growth and survival of cerebellar Purkinje cells in culture. *J. Neurochem.* **65,** 1551–1561 Medline

40. Schwarz, A., and Futerman, A. H. (1997) Distinct roles for ceramide and glucosylceramide at different stages of neuronal growth. *J. Neurosci.* **17,** 2929–2938 CrossRef Medline
41. Chiricozzi, E., Pomè, D. Y., Maggioni, M., Di Biase, E., Parravicini, C., Palazzolo, L., Loberto, N., Eberini, I., and Sonnino, S. (2017) Role of the GM1 ganglioside oligosaccharide portion in the TrkA-dependent neurite sprouting in neuroblastoma cells. *J. Neurochem.* **143,** 645–659 CrossRef Medline
42. Chia, P. H., Chen, B., Li, P., Rosen, M. K., and Shen, K. (2014) Local F-actin network links synapse formation and axon branching. *Cell* **156,** 208–220 CrossRef Medline
43. Flynn, K. C., Pak, C. W., Shaw, A. E., Bradke, F., and Bamburg, J. R. (2009) Growth cone-like waves transport actin and promote axonogenesis and neurite branching. *Dev. Neurobiol.* **69,** 761–779 CrossRef Medline
44. Hu, J., Bai, X., Bowen, J. R., Dolat, L., Korobova, F., Yu, W., Baas, P. W., Svitkina, T., Gallo, G., and Spiliotis, E. T. (2012) Septin-driven coordination of actin and microtubule remodeling regulates the collateral branching of axons. *Curr. Biol.* **22,** 1109–1115 CrossRef Medline
45. Spillane, M., and Gallo, G. (2014) Involvement of Rho-family GTPases in axon branching. *Small GTPases* **5,** e27974 CrossRef Medline
46. Kloos, A. D., Fisher, L. C., Detloff, M. R., Hassenzahl, D. L., and Basso, D. M. (2005) Stepwise motor and all-or-none sensory recovery is associated with nonlinear sparing after incremental spinal cord injury in rats. *Exp. Neurol.* **191,** 251–265 CrossRef Medline
47. Kuo, C. L., van Meel, E., Kytidou, K., Kallemeijn, W. W., Witte, M., Overkleeft, H. S., Artola, M. E., and Aerts, J. M. (2018) Activity-based probes for glycosidases: profiling and other applications. *Methods Enzymol.* **598,** 217–235 CrossRef Medline
48. Akiyama, H., Sasaki, N., Hanazawa, S., Gotoh, M., Kobayashi, S., Hirabayashi, Y., and Murakami-Murofushi, K. (2011) Novel sterol glucosyltransferase in the animal tissue and cultured cells: evidence that glucosylceramide as glucose donor. *Biochim. Biophys. Acta* **1811,** 314–322 CrossRef Medline
49. Marques, A. R., Mirzaian, M., Akiyama, H., Wisse, P., Ferraz, M. J., Gaspar, P., Ghauharali-van der Vlugt, K., Meijer, R., Giraldo, P., Alfonso, P., Irún, P., Dahl, M., Karlsson, S., Pavlova, E. V., Cox, T. M., *et al.* (2016) Glucosylated cholesterol in mammalian cells and tissues: formation and degradation by multiple cellular β-glucosidases. *J. Lipid Res.* **57,** 451–463 CrossRef Medline
50. Halling, K. K., Ramstedt, B., and Slotte, J. P. (2008) Glycosylation induces shifts in the lateral distribution of cholesterol from ordered towards less ordered domains. *Biochim. Biophys. Acta* **1778,** 1100–1111 CrossRef Medline
51. Ly, P. T., Singh, S., and Shaw, C. A. (2007) Novel environmental toxins: steryl glycosides as a potential etiological factor for age-related neurodegenerative diseases. *J. Neurosci. Res.* **85,** 231–237 CrossRef Medline
52. Lingwood, D., and Simons, K. (2007) Detergent resistance as a tool in membrane research. *Nat. Protoc.* **2,** 2159–2165 CrossRef Medline
53. Vu, H. S., Shiva, S., Hall, A. S., and Welti, R. (2014) A lipidomic approach to identify cold-induced changes in Arabidopsis membrane lipid composition. *Methods Mol. Biol.* **1166,** 199–215 CrossRef Medline

**Species-specific differences in nonlysosomal glucosylceramidase GBA2 function underlie locomotor dysfunction arising from loss-of-function mutations**

Marina A. Woeste, Sina Stern, Diana N. Raju, Elena Grahn, Dominik Dittmann, Katharina Gutbrod, Peter Dörmann, Jan N. Hansen, Sophie Schonauer, Carina E. Marx, Hussein Hamzeh, Heinz G. Körschen, Johannes M. F. G. Aerts, Wolfgang Bönigk, Heike Endepols, Roger Sandhoff, Matthias Geyer, Thomas K. Berger, Frank Bradke and Dagmar Wachten

*J. Biol. Chem. 2019, 294:3853-3871.*
*doi: 10.1074/jbc.RA118.006311 originally published online January 20, 2019*

---